CWP-083
August 1989
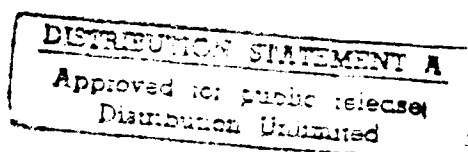
Common Shot, Prestack Inversion and

Mode Conversion Analysis of

Physical Model Seismic Data

by

Mark Jeffrey Emanuel

— Master's Thesis —

Center for Wave Phenomena
Department of Mathematics
Colorado School of Mines
Golden, Colorado 80401
Phone (303) 273-3557

TABLE OF CONTENTS

ABSTRACT

Imaging physical model data provides a good test for an inversion algorithm. The physical model data are real wave fields and do not include the simplifications of synthetic data. Also, the parameters of the model are known beforehand so that it is easy to determine how well the inversion works. Here, inversion is a true amplitude Kirchhoff depth migration in the sense that the amplitude of the imaged reflections is proportional to the reflection coefficient. Each shot record in a physical model data set is inverted separately with a common shot, prestack inversion routine with a laterally and depth variable velocity function. Each shot record inversion forms a partial image of the subsurface. The results are then stacked to form a full image of the subsurface. The physical model data set is inverted twice. For the second inversion, the output trace spacing is half the spacing for the first inversion and the output aperture is three times wider than in the first inversion. In both cases, the background velocity field is nearly identical to the actual model. This tests the inversion procedure independent of velocity analysis. Both inversions accurately position reflectors in the model but each performs better on different portions of the data. With a larger inversion output zone, steeper events are imaged better but the increased migration "smile" noise obliterates some deeper events. Both inversions are superior to a migration of the data performed by Marathon Oil Company. Velocities and densities of the model were estimated from the inversion amplitudes. The estimated velocities from the two uppermost reflectors agreed within ten precent of the true velocities but the estimates degraded with the deeper reflectors. The accuracy of the density estimates could not be determined because the true densities were unavailable.

The physical model data are also analyzed for doubly mode-converted reflections. The data are dip filtered to try to separate any mode converted reflections from primary compressional wave reflections. Stacking velocity analysis is used to determine whether the dip-filtered data contain any mode converted reflections. No mode converted energy is evident in the data.

i

LIST OF FIGURES

Figure

iii

GLOSSARY

Symbol	Definition
A	WKBJ Green's function amplitude
β, β_1	Inversion operators
b	Spatial kernel of β
c	Compressional wave velocity
F	Amplitude response of a bandpass filter
γ	Singular function of a surface
p	Ray parameter
R	Angularly dependent reflection coefficient
σ	Running parameter along rays
θ	Incidence angle
τ	Intercept time
T	Traveltime function
U_s	Scattered data
x	Distance
z	Depth

1. INTRODUCTION

A physical-model seismic experiment is a scaled down laboratory simulation of a real seismic survey and thus physical model data are an analog of a seismic survey over a simplified, known earth. The data are collected at ultrasonic frequencies with distances and time in the laboratory experiment scaled so that the distances, time, frequencies, and medium velocities are reasonable for real seismic data.

These data are useful for testing and comparing seismic data imaging techniques (migration/inversion). Seismic data modeling and imaging methods are based on theory that incorporates simplifying assumptions about the wave field. If an imaging procedure is based on the same theory as the modeling procedure, the imaging procedure is merely the inverse of the modeling procedure, and thus while the imaging may work perfectly on synthetic data from the modeling, it might not work well on field data. Physical model data do not introduce this problem; the data are real wave fields as are field data. The model data contain all wave effects, including head waves, near-field effects, mode conversions, and diffractions, that may have been omitted in the synthetic modeling. Testing imaging techniques on model data gives a better indication of how the techniques will perform on field data. However, because the models are simpler than the real earth and the physical parameters are known, it is easy to verify how well the imaging techniques accomplish what their intended goal of accurately imaging the subsurface.

Marathon Oil Company, which prompted this research, has generated physical model data which it has sent to contractors to evaluate their imaging (migration) techniques. The true velocities are known beforehand, so they can be used as the migration background velocity function. With this information, the migration techniques can be compared independent of the errors associated with imperfect knowledge of velocity. Marathon donated a physical model data set to the Center for Wave Phenomena so that we might try our inversion on the data. The model is structurally complicated enough to warrant prestack inversion. The first part of this thesis shows the application of Dong's (1989) common shot, $c(x,z)$, prestack inversion routine to the physical model data. The term $c(x,z)$ means that the input velocity varies laterally and vertically. I will show that this inversion method provides an accurate reflector map of the model and compares favorably to migrations of the same data by other methods.

1.1 Description of the Physical Model Data

The data, collected at the Seismic Acoustics Laboratory (SAL) at the University of Houston for Marathon Oil Company, will be referred to as the Marathon data. The data were collected over a block model in a water tank (Figure 1.1). Geologically, the model represents a salt ridge over a rifted basement. The top layer shown in Figure 1.1

was water. (Note that the velocity for the first layer, $v_p = 11750$ ft/s, is the scaled velocity, hence the difference from the true water velocity.) The lower layers, the actual block, were various epoxy resins. The high velocity, $v_p = 22410$ ft/s, third layer is the modeled salt ridge. SAL provided the scaled compressional wave velocities, v_p. I did not know the densities or shear wave velocities, except for the top layer, because it is water. Water's density is 1 g/cm^3 and its shear wave velocity is zero. The model varies only slightly in the out-of-plane (i.e. y) direction so that the 2.5-D assumption used later for deriving the inversion operator should be adequate for these data. The dimensions in Figure 1.1 are labeled with feet instead of scale feet. For brevity, I will use feet and seconds instead of scale feet and scale seconds throughout this thesis.

Figure 1.2 depicts the recording geometry of each shot record from the Marathon data. The data consist of 291 shot records. For each shot there were 48 receivers in an end-on spread to the right of the shot. The near receiver offset was 800 ft and the receiver spacing was 80 ft, so the far receiver offset was 4560 ft. The shot spacing was also 80 ft, with the first shot located at $x = 0$ ft and the last was at $x = 23200$ ft. Although the shots and receivers were at the depth $z = 0$ ft shown in Figure 1.1, this is not the water surface. They were submerged sufficiently so that no reflections from the water surface were recorded. For each shot, two seconds of data were recorded sampled at 4 ms. The recording filter passed frequencies between 2 and 60 Hz.

Figure 1.3 is a sample shot record. Automatic gain control (AGC) has been applied for the display to aid in viewing events. The shot location is $x = 2000$ ft, and the receiver spread extends from $x = 2800$ to $x = 6560$ ft. After the earliest event, the direct wave, the first curved event is the water bottom reflection. Reflections from the second and third interfaces are the next two events, and the strong event at about 1.45 s is a reflection from the model bottom. The reflection from the sawtooth interface does not produce an easily identifiable event on this record.

1.2 2.5-D Inversion Theory

In this section I will briefly outline the theory used for inverting the Marathon data. More detailed descriptions of the theory may be found in Dong (1989), Bleistein (1987), Bleistein et al. (1987), Docherty (1987), Sullivan and Cohen (1987), and Cohen et al. (1986). Inversion and migration have the same goal: imaging reflectors in their proper location. The philosophies of the techniques, however, differ.

Zero-offset migration takes advantage of the exploding reflectors model. This model has two aspects. First, the earth velocities are replaced by velocities one half the true value. Second, at time zero, the reflectors "explode" to generate an upgoing wave field, which is recorded at the surface. These exploding reflector data are an approximation of the data that would be recorded in a true zero offset experiment. To migrate the zero-offset data, the data are extrapolated downward to all output depth levels using the half velocity of the exploding reflectors model. This is a transformation of the data to what would have been recorded if the receivers were at depth. At each

depth level, the data are imaged at time zero (when the reflectors explode). This produces a migrated image of the subsurface. For prestack migration, the receiver and source data are both downward extrapolated and the data are imaged at time zero. At time zero, a receiver coincident with a source will show a reflection if the receiver and source are on a reflector. Different types of migration, such as Kirchhoff, finite difference, and Stolt, all follow this downward extrapolation and imaging procedure. The methods differ in their approximations to the wave field extrapolator and in the domain ($t-x$ or $\omega-k$) in which extrapolation is applied. More details on migration may be found in Claerbout (1985) or Yilmaz (1987).

The inversion operator is derived from the solution of the forward problem. An integral representation of the scattered data is obtained by solving the acoustic wave or Helmholtz equation. Either the Kirchhoff or Born approximation is used in solving the forward problem. I will describe the method of deriving the inversion operator when the Kirchhoff approximation is used. The Green's functions in the representation are replaced by the WKBJ approximation because seismic data are high frequency. That is, the length scales of interest in the medium, such as depth to the reflector, radius of curvature of the reflector, etc., are much larger than the nominal wavelength in the data. The forward scattered data then have the representation

$$U_s(\omega,\xi) = i\omega \int dx' A(x',\xi) e^{i\omega T(x'.\xi)} \ , \tag{1.1}$$

when the Kirchhoff approximation is used. In equation (1.1) the x' integral is over the reflecting surface. ξ is a parameterization of the source and receiver coordinates x_s and x_r. $A(x,\xi)$ is a specific amplitude term defined by the theory. It includes spreading and transmission losses. $T(x,\xi)$ is the sum of traveltimes from the subsurface point to the source and the subsurface point to the receiver:

$$T(x,\xi) = t(x,x_s) + t(x,x_r) \ \ .$$

When the Born approximation is used, the $i\omega$ in equation (1.1) is replaced by ω^2, the x' integral is over volume, and the kernel A is different.

Equation (1.1) has mathematical form similar to a Fourier transform. From experience with Fourier transforms and the migration concept of propagating the source and receivers backward, an educated guess would be that the phase of the inversion operator would be the opposite that of the forward solution. The three dimensional inversion formula is

$$\beta(x) = \int d\xi \, b_{3D}(x,\xi) \int d\omega \, F(\omega) e^{-i\omega T(x.\xi)} \, U_s(\omega,\xi) \ \ . \tag{1.2}$$

In equation (1.2), $F(\omega)$ is a bandpass filter to recognize the bandlimited nature of

seismic data. $F(\omega)$ is the product of the amplitude spectra of all filters applied to the data. This includes the source wavelet, receiver effects, recording instrument filters, and any processing filters. The amplitude factor, $b_{3D}(x,\xi)$, is determined by substituting for U_s from equation (1.1) and requiring that the inversion output, $\beta(x)$, be asymptotically equal to the reflection coefficient for the output point, x, on the reflector. This amplitude factor corrects the amplitude of the data for divergence and transmission losses and is different for different sortings of the data. That is, b_{3D} for data sorted into common-offset gathers is not the same as b_{3D} for common-shot gathers.

The inversion operator, defined by equation (1.2), is essentially a Kirchhoff migration operator with a special amplitude weight. Careful attention is paid to the amplitude in deriving the forward solution and the inversion operator so that the amplitude in the results can be faithfully diagnostic of characteristics of the medium.

Equation (1.2) is the 3-D inversion formula. Most seismic data, however, are collected in 2-D lines. For a single seismic line, we cannot expect to be able to correctly image any reflection from outside the plane of the survey. We, therefore, assume that the earth velocity varies only in the plane directly beneath the data line and has no out-of-plane variation. This is equivalent to assuming that the seismic line was shot along the dip direction. Seismic sources, however, are point sources and this necessitates the use of 3-D Green's functions that take three-dimensional spreading into account. This situation with 2-D data and 3-D (i.e., point) sources is called 2.5−*dimensional*.

To convert the 3-D inversion formula, equation (1.2), to 2.5-D, the integral for the out-of-plane ξ−direction is evaluated by stationary phase. Stationary phase is a method for asymptotic evaluation of Fourier-like integrals Bleistein (1984), valid under the assumption the data are high frequency. After the stationary phase approximation has been applied, we obtain the 2.5-D inversion formula:

$$\beta(x) = \int d\xi\, b(x,\xi) \int d\omega\, F(\omega) \sqrt{i\omega}\, e^{-i\omega T(x,\xi)}\, U_s(\omega,\xi) \quad , \tag{1.3}$$

where $\sqrt{i\omega} = \sqrt{|\omega|}\, e^{i\mathrm{sgn}(\omega)\pi/4}$. This factor arises in the stationary phase evaluation and provides the proper phase for the inverted data.

As stated earlier, the inversion asymptotically gives the geometric optics reflection coefficient when the output point is on the reflector. That is,

$$\beta(x) \sim R[x,\theta(x)]\cos\theta(x)\,\gamma_B(x) \quad , \tag{1.4}$$

where $R[x,\theta(x)]$ is the angularly dependent reflection coefficient and $\gamma_B(x)$ is the bandlimited singular function of the reflector. It is important to note that the inversion output gives the reflection coefficient at only one angle for a single output point. This is the angle for which a specular reflection from this point could be recorded given the

- 4 -

shot and receiver geometry. Therefore, θ is a function of x but I will usually not indicate this dependence. That is, I will use θ to mean $\theta(x)$.

The singular function of the reflector is a Dirac delta function that has its support on a surface (Bleistein, 1984). For a surface S, let σ be the signed normal distance from S. Then, the singular function is defined as $\gamma(x) = \delta(\sigma)$. On the surface,

$$\gamma_B(x)\Big|_S = \delta_B(\sigma)\Big|_{\sigma=0}$$

$$= \int F(\omega)\, d\omega \quad . \tag{1.5}$$

Therefore, the inversion output for a point on the reflector is

$$\beta(x) \sim R(x,\theta)\, \cos\theta \int F(\omega)\, d\omega \quad , \tag{1.6}$$

and for a point not on a reflector it decays as the reciprocal of the distance to the reflector.

I used the operator defined by equation (1.3) to invert the Marathon data. The implementation of the operator is described in Chapter 2. Further details may be found in Dong (1989).

1.3 Why Mode Conversion?

Shear wave (S-wave) applications to exploration have increased in the last decade. Shear wave surveys can now help determine anisotropy or can be used for direct hydrocarbon detection (Tatham and Stoffa, 1976; Meissner and Hegazy, 1981; Robertson and Pritchett, 1985; Neidell, 1985). Marine shear wave surveys may also have applica ons in seabed mapping.

On land, shear waves can be generated and recorded directly and easily. Since water cannot support shear waves, marine S-wave surveys, however, are difficult to conduct. Marine shear wave data can be collected by two methods. The first is to place the source and receiver on the seabed and directly generate and receive shear waves as on land. This method is limited to shallow water (Neidell, 1986). The other method involves generating compressional waves (P-waves) in the water, which, at the seabed, can convert to shear waves. The shear waves may then be scattered back to the seabed and subsequently converted back to compressional waves in the water, which are recorded near the surface. I will refer to waves that are mode-converted from compressional to shear, scattered, and then mode-converted back to compressional

as PSSP waves (Figure 1.4). P-wave reflections will be referred to as PP. One P for the downward leg, and the second for the upward.

The PSSP type of survey has the advantage that it can be conducted like a standard marine seismic survey with a few differences mentioned below. This allows the data to be collected much more quickly and efficiently than by the sea bottom detector method. One difference of the PSSP survey from a standard marine survey is that, because shear waves travel slower than P-waves, recording times must be longer to record reflections from the same depth as in a standard P-wave survey. Also, long offsets are required because the strongest mode conversion occurs for incidence angles greater than the P-wave critical angle. (This will be shown in Chapter 3). Shallow water is helpful because it decreases the offset required for reaching the critical angle of incidence, but the water depth does not have to be as shallow as in the water bottom method. Also, the higher the P-wave velocity of the water bottom the smaller the critical angle and thus shorter offsets are needed, and the greater the shear velocity of the water bottom, the greater the energy in mode-converted waves.

The PSSP type of marine shear wave survey has two major disadvantages over the sea-bottom receiver survey. First, since the P- and S-wave energy are both recorded as P-waves, the two must be separated during processing. The separation, based on move-out velocities, will be discussed in Chapter 3. The second disadvantage is that the polarization of the S-waves is lost when they are converted to P-waves at the water bottom. S-wave polarization is useful for determining anisotropy.

I had originally intended to derive an inversion for PSSP waves and use it to invert the Marathon data. Before I could perform an inversion, however, I needed to ascertain whether the data contained significant mode-converted energy. Chapter 3 describes the methods I used to search the data for PSSP events. I conclude that the data do not contain significant mode-converted energy. The offsets need to be longer to record PSSP energy. Without the PSSP waves contained in the data, the inversion for mode-converted energy is impossible.

2. COMPRESSIONAL WAVE INVERSION

This chapter will describe the inversion of the Marathon data for compressional waves. The data were inverted using the prestack, common shot, variable background inversion method of Dong (1989). The first part of the chapter will describe the implementation of Dong's inversion routine. The next part will discuss several inversions with different parameters. Only the kinematics, that is, the positioning of the reflectors (Aki and Richards, 1980), of the inversions will be considered in this part. I will discuss parameter estimation from the inversion amplitudes (i.e., dynamics) in the last part of the chapter.

2.1 Common Shot, $c(x,z)$ Inversion

In this section, I will briefly describe Dong's (1989) common shot, $c(x,z)$ implementation of the general 2.5-D inversion formula, equation (1.3). To accommodate the generality that $c(x,z)$ implies, the traveltime function, T, and the amplitude kernel, b, are computed by tracing rays from the output point to the source and receiver locations. The ray tracing scheme (Docherty, 1987) requires constant-velocity layers bounded by interfaces that are continuous and have continues first and second derivatives. Also, each interface must continue across the whole line and its depth must be a single-valued function of distance. To model a pinch out, a layer must become very thin, but maintain finite thickness.

As mentioned in Chapter 1, the amplitude kernel, b, depends on the source-receiver geometry. For common-shot data,

$$b(x,\xi) = \frac{\sqrt{1/\sigma_s + 1/\sigma_r} \; |\partial\alpha(\xi)/\partial\xi|}{2(2\pi)^{3/2} \; A(x,x_s)A(x,\xi)} \tag{2.1}$$

(Dong, 1989). In equation (2.1), σ_s and σ_r are running parameters along the rays for which $|dx/d\sigma|^2 = 1/c^2$. α is the takeoff angle of the ray at the receiver location ξ, and its derivative is the in-plane spreading factor. $A(x,x_s)$ and $A(x,\xi)$ are the WKBJ amplitudes for rays from the output point to the source and from the output point to the receiver, respectively. The WKBJ amplitudes involve transmission coefficients and spreading factors, and are never zero.

The first step of the inversion is to Fourier transform the data by Fast Fourier Transform (FFT). The ω-integral of the inversion operator,

$$\int d\omega \, F(\omega)\sqrt{i\omega} \, e^{-i\omega T(x,\xi)} \, U_s(\omega,\xi) \;, \tag{2.2}$$

is the next step. It constitutes filtering and an inverse Fourier transform of the data. Equation (2.2), also evaluated by FFT, yields a table of the data indexed by time. These steps are independent of the output point so they need be done only once, to "preprocess" the data prior to doing the remainder of the inversion.

The next step is the ξ-integral,

$$\beta(x) = \int d\xi \, b(x,\xi) \, u_p(\xi) \ , \tag{2.3}$$

where $u_p(t,\xi)$ is the preprocessed data. The receiver locations are discrete so this integral is really a summation over receiver. The amplitude and traveltime functions are determined by tracing rays from the output point to the source and to each receivers. For each trace, the data value indexed by the traveltime for that receiver is linearly interpolated from the preprocessed data and then multiplied by the amplitude function. The weighted data values from all traces are summed for the inversion output. This is repeated for every desired output point. The inversion algorithm may be summarized by the following pseudo-code block:

> *Preprocess data*
> *For each output point {*
>
> > *Set sum to zero*
> > *Trace ray from output point to source*
> > *For each receiver {*
> >
> > > *Trace ray from output point to receiver*
> > > *Get data value corresponding to traveltime*
> > > *Weight data value by amplitude*
> > > *Add weighted value to sum*
> > > *}*
> >
> > *}*

This inversion procedure is applied to each shot record separately. For each shot record, a partial image of the subsurface is formed. To obtain a complete image, the inversion of each shot record must be stacked on output location. Proper reflector images will stack in phase, but the impulse response "smiles" and noise will not. At best, the smiles will overlap slightly and cancel each other. At worst, they will not overlap but will be lower order than the reflector images that stack constructively.

Stacking, however, destroys the amplitude information in the inversion. Any parameter estimation from the inversion amplitudes must be done using the unstacked inverted data.

2.2 Inversion of the Marathon Data

In this section, I describe the application of Dong's routine to the Marathon data, concentrating on the kinematics of the inversion. I inverted the Marathon data twice with different parameters and background velocity models. Finally, I will compare the inversion results to migrations of the same data performed by two different methods.

2.2.1 First Inversion

All migration and inversion techniques require an estimate or guess about the medium velocity. The input velocity function for the Marathon inversion was nearly the true velocity function shown in Figure 1.1 with the interfaces bounding the constant-velocity layers defined by a cubic spline fit to control points obtained by digitizing the cross section. In Figure 2.1, the interfaces shown are denoted by bandlimited delta functions (i.e., sinc functions) centered at the proper depths for each interface. (Note that the bandlimited delta function in Figure 2.1 is a function of depth rather than normal distance, as is the singular function of the reflector.) The trace spacing in Figure 2.1 is 80 ft. By letting the second layer become thin (down to 30 ft, over the dome), the pinch out is modeled.

The input velocity function is similar to the actual model but not exactly the same. The spline fit causes small unwanted bumps on the interfaces where the control-point spacing is too fine. The most notable of these is at the base of the fault cutting the third interface. Also, Marathon had indicated on the cross-section provided with the data that there was some uncertainty as to the true structure near the salt dome flanks.

The first version of the inversion program required that the number of output traces be the same as the number of input traces. Therefore, each shot inversion yielded 48 output traces. To image steeper events I chose the output trace spacing to be 160 ft, twice the receiver spacing. This gives a larger output than input area so that events do not migrate out of the section. The depth sampling interval was 40 ft, with the first sample at zero depth. There were 301 depth samples, so the last sample was at 12000 ft. The first output trace was located at the shot position, and the other traces were to the right of the shot. The farthest trace was, therefore, offset 7520 ft to the right of the shot location.

To save computing time, rays were not traced from every output point to every receiver. Instead, rays were only traced from every point on every fifth output trace to every fifth receiver. The program linearly interpolates amplitude and traveltime functions from the values obtained by the ray tracing. This should not degrade the results appreciably, because the traveltime function varies slowly.

Figure 2.2 is the inversion of the shot record shown in Figure 1.3. (Note that Figure 1.3 shows the shot record after AGC. The inversion is applied to the ungained

record.) The smeared event at depths less than 1000 ft is from the direct arrival. Muting the direct arrival would have eliminated this noise. The events in Figure 2.2 at 3000 ft, 4500 ft, and 6300 ft are partial images of the first three interfaces. The event at 11200 ft corresponds to the model bottom. The fourth reflector, the sawtooth, is faint and located at a depth of 9000 ft and distance of 6000 ft.

An inversion similar to Figure 2.2 was obtained for all 290 shot records. Each yields a different partial image of the subsurface. I sorted the inversions on the output trace location and stacked them to form a full image of the subsurface. (depths less than 1300 ft are muted to eliminate the direct arrival noise). After stacking, the output trace spacing is 80 ft. Figure 2.3, the ungained stack of all the individual shot inversions, contains several interesting features. The reflectors stack constructively and are imaged well, whereas the concave upward, migration impulse response smiles (also known as "migration smiles") stack destructively and are not noticeable. Also, the amplitude of the deeper reflectors is less than the amplitude of the shallower reflectors. This decay in amplitude is also noticeable in the shot inversion, Figure 2.2, and will be discussed in Section 2.3.

Stacking the shot inversions degrades the amplitude information. Parameter estimation from the amplitudes must be done before stacking (Bleistein and Cohen, 1989). Because the amplitudes in Figure 2.3 have little meaning, no harm is done by applying gain to see the lower reflectors better. Figure 2.4 is the stacked section of Figure 2.3 after applying AGC with a 200-sample window. The gain has also enhanced noise in addition to the deeper reflectors, but the noise level is still relatively low.

Comparing Figures 2.4 and 1.1 show that the reflectors have been correctly positioned. Only slight differences occur between the cross section and the inverted data. Most of these are near the dome flanks where the cross section is in error. Overall, the inversion performs well in locating the reflectors, with only a few problems and shortcomings. The images of the steep dome flanks and fault planes and the left portion of the leftmost sawtooth are weak. Finally, the model bottom image has breaks at distances 8500 ft and 14000 ft, and it is not perfectly flat as it ought to be. The second inversion was done to try to remedy some of the shortcomings of this result.

To understand why the steep flanks are imaged weakly, consider an experiment in a constant velocity medium with a single reflector and a single source and receiver. The envelope of all reflectors having the same reflection time is the familiar reflection ellipse with the source and receiver at the foci (Figure 2.5). If the reflector has zero dip, the specular point lies below the midpoint of the source and receiver. As the reflector dip increases, the specular point moves farther up dip and laterally away from the midpoint. Consequently, imaging only in a region near the source and receiver, as with this particular example inversion, discriminates against steep dips. The flanks could be imaged better by increasing the output range. Because the program originally limited the number output traces, the output range could only be increased by increasing the output trace spacing. This, however, would have led to aliasing the steeper events, the very event sought after with the increased output range. Another option would be to invert the data several times with different output zones. This was

more difficult, however, than changing the program.

The weak image of the left sawtooth is not the fault of the inversion. Instead, it is due to the recording geometry. The left portion of the sawtooth was not illuminated by the rays in the common-shot gathers and, hence, no reflections from it were recorded. Therefore, the left part of the leftmost sawtooth image is weak.

The remaining problems are probably due to inaccuracies of the background velocity model. The breaks in the bottom image occur directly beneath sawtooth faults, where the output is particularly sensitive to inaccuracies in the model. The wobble in the model bottom image is also the result of slight inaccuracies elsewhere in the model.

2.2.2 Second Inversion

The background velocity function and several inversion parameters were changed for the second inversion to improve the image. Figure 2.6 shows ray tracing in the first background velocity function from a subsurface point to equally spaced points on the surface. The bumps from the spline fit cause the local normal to deviate from the true normal. This causes the raypaths to be distorted so that the traveltime function is not smooth. To smooth the interfaces, some control points have been removed. Figure 2.7 shows the interfaces for the second background velocity function. The layer velocities are unchanged, but the spline- caused bumps on the interfaces in Figure 2.1 have been removed in Figure 2.7. Figure 2.8 is a ray tracing plot from the same subsurface point as in Figure 2.6, but using the second background velocity function. Notice that the raypaths are not distorted; as a result, the traveltime function should be much smoother and thus the inversion image should be improved.

Some parameters were also changed for the second inversion. The program was altered so that the user could specify the number of output traces. For shot records with $x_s < 12000$ ft, the second inversion created 300 output traces spaced at 80 ft giving an image of the whole model. To image the left edge of the model from shot records on the right half of the model (i.e., $x_s > 12000$ ft), rays had to cross the second interface twice. The ray tracing routine did not allow this. Therefore, for shot records on the right half of the model, 150 traces were generated with the first trace located at $x = 12000$ ft. The inversion of these shots gave an image of the right half of the model. The increased inversion output aperture should allow reflectors of any dip to be imaged as long as the reflections are recorded in the data and are not aliased.

The other parameter change concerned the ray tracing interpolation. Instead of tracing rays from every point on every fifth output trace to every fifth receiver, rays were traced from every point on every second output trace to every second receiver. This was done to achieve as accurate an image as possible. As a result, the second inversion of all shot records took 3.5 times as much CPU time as the first.

Figure 2.9 is the inversion of the shot record shown in Figure 1.3. The inversion covers the whole model although the imaged portion of the reflectors is limited to a small zone. The result is similar to that in Figure 2.2. The output outside the zone where the reflectors are imaged consists of migration-smile noise. The noise is lower order so that it is not as visible.

Inversions from nearly all shot records were stacked to form a complete image of the model. The inversions from a few shot records were lost due to computer failures. The stacked image after AGC is shown in Figure 2.10. Compared to Figure 2.4, there are some improvements and also some disappointments. As expected, the steep flanks of the dome are better imaged. They appear steeper than in the cross-section in Figure 1.1. As mentioned previously, the cross-section is incorrect near the dome flanks. The flanks are probably as steep as the inversion depicts them. The fault plane of the third interface has also been imaged.

The main disappointment in this inversion is the large degree of migration smile noise. Migration smiles occupy more area in the shot inversion than do the reflector images. Because some shot inversions were missing, their contribution to the destructive stacking of the smiles was lost and, consequently, the smiles are not attenuated as much. The noise has nearly obliterated the fifth tooth in the fourth (sawtooth) interface. Selective windowing of the shot inversions to eliminate smile noise before stacking would result in an image with lower noise and enhanced steep events.

The first inversion images the deeper events better because the inversion output contains fewer smiles. This is partly a result of the narrower output aperture. The second inversion images the steeper events better, particularly the dome flanks, because of the wider output aperture. The inversion parameters can be tuned to give the optimum image for a particular imaging goal (and exploration target).

2.2.3 Migrations of the Marathon Data

In this section, I will compare the kinematic imaging of the common shot inversion to migrations of the same data by two different methods. Figure 2.11 is a poststack, finite-difference, time migration from the University of Houston. Detailed comparisons of time migrations and depth migrations are not fair but general comparisons may have some value. Figure 2.12 is a prestack, finite-difference, depth migration from Marathon Oil Company. Comparing Dong's prestack depth inversion to another prestack depth migration is the best method to determine its relative performance.

Compare Figure 2.11, the time migration, to Figures 2.4 and 2.10. Figure 2.11 shows much pull up in the center of the section because it is a time migration. Figures 2.4 and 2.10 do not show any pull up because they are sufficiently accurate depth migrations. The pull up is not a valid point of comparison. Also, the location of reflectors cannot be compared. The next two points, however, are legitimate. The fourth and fifth teeth of the sawtooth interface are invisible in the time migration. In

both inversions, the fourth sawtooth is imaged while the fifth is imaged in Figure 2.4. Also, the time migration shows two crossing events at the peak of the dome. Figure 1.1 shows that there ought to be only one event. Both inversions show only one event at the peak of the dome. For these two points, at least, the inversions image the model better than does the time migration.

Now compare Figure 2.12, the depth migration, to Figures 2.4 and 2.10. The migration contains more noise than do the inversions. Also, the migration images the steep flanks of the dome poorer than even the first inversion (Figure 2.4). Both inversions image the fourth sawtooth well, whereas the depth migration images it poorly. In the migration, the fifth sawtooth is completely absent. The first inversion (Figure 2.4) images it well. In the second inversion (Figure 2.10), it is obscured by noise but still present. The inversion imaged the model better than the depth migration did. This may be due to poor parameter choice for the depth migration rather than a failing of that migration method.

2.3 Parameter Estimation from Inversion Amplitudes

Up to this point, only the kinematics of the inversion have been discussed. The main advantage of inversion is that it better "corrects" the reflection amplitudes. Equation (1.6) gives the relationship between the inversion amplitude and the angularly dependent reflection coefficient. The acoustic reflection coefficient is given by

$$R(x,\theta) = \frac{\dfrac{\cos \theta}{c} - \dfrac{\cos \theta_1}{c_1}}{\dfrac{\cos \theta}{c} + \dfrac{\cos \theta_1}{c_1}}$$

$$= \frac{\dfrac{\cos \theta}{c} - \left[\dfrac{1}{c_1^2} - \dfrac{\sin^2\theta}{c^2} \right]^{1/2}}{\dfrac{\cos \theta}{c} + \left[\dfrac{1}{c_1^2} - \dfrac{\sin^2\theta}{c^2} \right]^{1/2}} \quad , \tag{2.4}$$

where c and c_1 are the medium velocities above and below the reflector, θ is the incidence angle, and θ_1 is the acute angle between the normal to the reflector and the propagation direction of the refracted wave in the lower medium (Bleistein, 1987). Solving equation (2.5) for c_1 gives:

$$c_1 = c \left[1 - \frac{4R\cos^2\theta}{(1+R)^2} \right]^{-1/2} \qquad (2.5)$$

The peak value of the inversion amplitude is the product of the reflection coefficient, the cosine of the particular specular angle of incidence at the output point, and the area under the effective filter of the data. The effective filter is the product of all filters applied to the data. To estimate the velocity of the medium below an interface, one needs to know the velocity above the interface, the specular angle, and the area under the filter. (This assumes that the density does not vary across the interface.) It is typical to start with a known velocity near the surface and estimate the velocity downward across reflectors, working progressively deeper into the section. The upper medium velocity can be taken as known. The specular angle, however, is not known *a priori*.

Bleistein (1987) describes a method for determining the specular angle. Another inversion operator can be constructed by a minor modification of the original inversion operator kernel: the old amplitude term is divided by the sum of the gradients of traveltimes to the source and receiver. Bleistein calls this new inversion operator β_1. The peak value of this operator is given by

$$\beta_1 \sim R(x,\theta) \int F(\omega)\,d\omega \quad . \qquad (2.6)$$

The ratio of the peak values of β and β_1 gives the cosine of the specular angle. The inversion routine can easily be modified to output both β and β_1 simultaneously at virtually no additional cost.

Because of time constraints, I could only invert the one shot record in Figure 1.3 with both β and β_1. The output trace spacing was 80 ft, and 48 output traces were created. It was not necessary to have a large inversion output zone for this shot record because I knew from the earlier inversions (Figures 2.2 and 2.9) where the reflectors would be imaged. The background velocity model and ray tracing interpolation parameters were the same as for the second inversion (Section 2.2.2). Figure 2.13 is the β inversion of the shot record. The β_1 inversion looks the same but is scaled differently.

First consider the uppermost reflector. The first task is to get the peak values on the reflector, assuming that the effective filter of the data is a zero-phase, bandlimited, delta function. The wavelet of the data, however, is not zero phase. It is a doublet, and its peak value is not obvious; is it the absolute maximum of the positive lobe of the doublet, or of the minimum lobe, or some other value? For determining the specular angle, only the relative, not absolute, values of β and β_1 matter. After performing the ratio of the β and β_1, only the cosine remains. However, the absolute value of the inversion peak will be an issue when finding the lower medium velocity.

For finding the specular angle, I used the positive peak value. Because the peak value does not always fall on a sample point, I oversampled β and β_1 four times to get better estimates. The oversampling was done by FFT, padding the traces with zeros, and inverse FFT. The solid line in Figure 2.14 shows the inverse cosine of the ratio of the peak values of β and β_1 for the first reflector. In the zone where the reflector is illuminated, from approximately $x = 2400$ ft to $x = 4280$ ft, this ought to be the specular incidence angle. The dashed line is the theoretical specular incidence angle for the approximation that the first reflector is a flat plane at the depth of 2700 ft:

$$\theta = \tan^{-1}\frac{x}{2z} \quad ,$$

where $z = 2700$ ft. This is a valid approximation for this shot record (see Figure 1.1). The maximum error between the data incidence angle and the theoretical incidence angle is 3% for 2640 ft $< x <$ 3600 ft. The error increases near the endpoints of the illuminated zone, as expected. This method for determining the incidence angle gives good results for output points within the illuminated zone.

Next, I will describe how the area under the effective filter was calculated. I will consider the effective filter to have two parts, the data filter and the processing filter. The data filter is the net filter effect of the source signature, the subsurface (e.g. attenuation), the receiver, and recording filters. The processing filter is a trapezoidal bandpass filter with corner frequencies 2, 10, 50, and 60 Hz.

I assumed that the direct-arrival wavelet represents the data filter. This implies that the attenuation is negligible. To find the area under the data filter, I stacked the shot records from $x_s = 2000$, 4000, 6000, 14000, 16000, 18000, 20000, and 22000 ft for common offsets. I omitted the shots near the middle of the model because the water-bottom reflection interfered with the direct arrival. The stack was normalized by the number of traces stacked. Next, the first breaks were aligned and the data were truncated after 40 samples (160 ms). Next, the traces had to be corrected for spreading. The 3-D acoustic Green's function predicts decay of $O(1/r)$. Least squares fitting a curve of the form $y = A\,r^{-n}$ to the peak value of the amplitude spectrum of each trace showed that the first arrivals decay as $O(1/r^{0.8})$. I used the amplitude spectrum because the time samples do not fall on the same part of the wavelet on every trace. The frequency samples do fall on the same part of the spectrum, though. The least-squares fit for only the far-offset traces shows a decay of nearly $O(1/r)$. This indicates a near-field effect is causing the best-fit decay for the ensemble of all traces to deviate from $O(1/r)$. The piezoelectric transducer source for the physical model experiment is not a dilational, point source so inclusion of near field effects is valid even though water is an acoustic media. In the near field, decay is $O(1/r^2)$ (Lighthill, 1978). I applied the divergence correction by multiplying the traces by $\dfrac{4\pi r}{1 + B/(Ar)}$, where A and B are determined by least-squares fitting $y = \dfrac{A}{r} + \dfrac{B}{r^2}$ to the peak amplitude spectrum values. The ratio $B/A = -320$. For $r \gg |B/A|$, the

divergence correction factor approaches $4\pi r$, the standard, far-field correction.

The processing bandpass filter was applied to the divergence corrected traces and the area under the amplitude spectrum for each trace was computed by the trapezoidal rule. The areas were averaged to obtain the area under the effective filter.

Before the lower velocity can be estimated, the phase shift of the data wavelet must be compensated for. One method to do this is to apply a wavelet shaping filter to the data to convert the wavelet to zero phase before inversion. Another is to compensate after inversion. I used a post-inversion method. Let P be the peak (i.e., the positive maximum rather than the negative or absolute maximum) of the direct arrival wavelet and P_z be the peak of the zero-phase equivalent of the direct arrival wavelet. I will call the positive peak, or the equivalent negative peak for phase reversed reflections, the pseudo-peak. I multiplied the pseudo-peak value of the inversion, β_1, by the ratio P_z/P to give an approximation of what the amplitude would have been if the data wavelet were zero phase. Again, this implies the assumption that the filter effects of the subsurface are negligible. The ratio P_z/P was 1.4. If I had more time, I would have tried the wavelet shaping method and compared the results.

We now have all the necessary information to estimate the lower medium velocity using equation (2.5), where

$$R = \frac{\beta_1\,|_{peak}}{A_f} \quad .$$

Here, $A_f = \int F(\omega)\,d\omega$ and $\beta_1\,|_{peak}$ is the phase-compensated pseudo-peak of β_1. Estimating the second layer velocity using the β_1 values (after oversampling) for the first interface in the illuminated zone give approximately 22000 ft/s. This is an error of 40 percent. This poor estimate can be attributed to at least two reasons. First, equation (2.5) is for an acoustic reflection coefficient when there is no density contrast. The real model has density contrasts, and the seabed layer is elastic. Second, the source was directional. Styrofoam cups were positioned around the piezoelectric transducer source and receivers to reduce the direct arrival. Consequently, the calculated the area under the data filter using the direct arrival is too low causing the estimated velocity to be too high.

The acoustic reflection coefficient with density contrast is

$$R(x,\theta) = \frac{\dfrac{\cos\theta}{\rho c} - \dfrac{1}{\rho_1}\left[\dfrac{1}{c_1^2} - \dfrac{\sin^2\theta}{c^2}\right]^{1/2}}{\dfrac{\cos\theta}{\rho c} + \dfrac{1}{\rho_1}\left[\dfrac{1}{c_1^2} - \dfrac{\sin^2\theta}{c^2}\right]^{1/2}} \quad . \tag{2.7}$$

- 16 -

Equation (2.7) can be rearranged to yield:

$$\frac{(1-R)^2}{(1+R)^2}\frac{\cos^2\theta}{\rho^2 c^2} = \frac{1}{\rho_1^2 c_1^2} - \frac{\sin^2\theta}{\rho_1^2 c^2} \; . \tag{2.8}$$

Equation (2.7) is in the form of a line: $Y = a + bX$, where

$$Y = \frac{(1-R)^2}{(1+R)^2}\frac{\cos^2\theta}{\rho^2 c^2}$$

and

$$X = -\frac{\sin^2\theta}{c^2} \; ,$$

and both X and Y are known quantities. X and Y may be plotted and the unknowns, c_1 and ρ_1, can be determined from the slope and intercept of the best fit line.

Figure 2.15 shows Y versus X for the first interface and using the previously calculated area under the filter and assuming density of 1.0 g/cm^3 for the water. Only samples from the illuminated zone are plotted. The first sample in the illuminated zone is the end of the short "tail". As the incidence angle increases, the points move clockwise. Therefore, the points near the end of the long tail correspond to large incidence angles. Also plotted in Figure 2.15, is the "best fit" line. It appears that the "best fit" line should have negative slope to fit more points. The line, however, must have a positive slope for the lower density to be real, and is defined by only four points. The first, that is, right uppermost, point on the line corresponds to the first point in Figure 2.14 where the data and theoretical incidence angle curves match, and the last point lies near the middle of the range of good incidence angles. At least two reasons explain why the points that define the "best fit" line with positive slope are from the left part of the illuminated zone where the incidence angle is smaller. First, the acoustic approximation holds better for small incidence angles. At larger incidence angles, more mode-conversion occurs and equation (2.7) deviates more from the elastic P-wave reflection coefficient. Second, the recording aperture necessary for good amplitudes is smaller for shorter offsets, and hence smaller incidence angles. The recording aperture will be discussed again later in this section. For these data, the recording array was not long enough to give good inversion amplitudes for reflection points far from the source.

The density and velocity of the lower medium, determined from the slope and intercept of the line in Figure 2.15, are 0.90 g/cm^3 and 24000 ft/s. The velocity is too high because the area under the filter is too low. Figure 2.16 shows Y versus X for the first interface and with the area under the filter adjusted so that the estimated value of

the second velocity is correct. The estimated lower medium density is 0.85 g/cm^3.

I next used the adjusted area under the filter and the estimated density for the second layer to estimate the velocity and density of the third layer from the peak of β_1 on the second interface. Figure 2.17 is the X versus Y plot. Again, the line was fit for a positive slope. The estimated density and velocity for the third layer are 0.71 g/cm^3 and 20000 ft/sec. The velocity estimate error is 10 percent. This is a reasonable size error for real data.

Figure 2.18 is the X versus Y plot for the third interface. The true third layer velocity was used for computing X and Y. The velocity and density for the fourth layer corresponding to the line on the figure are 15800 ft/s and .97 g/cm^3. Finding the best fit line for Figure 2.18 is not well defined. One can imagine many lines fitting the data that would give densities and velocities with wide variation. Although the velocity estimate is good, the density estimate is not consistent with the density estimate from the first interface. The second layer and the fourth layer were constructed of the same material so the densities should be the same. I used the correct velocities for estimating parameters so that errors did not compound. The density estimates were used to estimate the parameters of the next layers; I did not know the true densities.

Finally the fourth interface gave estimates of the fifth layer velocity and density as 16800 ft/s and .78 g/cm^3. I used the true velocity and 0.85 g/cm^3 for the density of the fourth layer when estimating the fifth layer parameters.

Velocity estimates from the inversion of one shot record gave reasonable results. Because the model densities are unknown, the validity of the density estimates cannot be verified. Better accuracy could have been obtained by using the inversions from more than one shot. The multiplicity of data would have lessened the opportunity of error when fitting a line to the scatter plots. The velocity estimates degraded with depth because of limited recording aperture and compounding errors in density. The integration range for equation (2.3) should ideally run from $-\infty$ to $+\infty$. The actual integration range is determined by the receiver spread. The dominant contribution of (2.3) is from the specular point, with the endpoints of integration the next most dominant contribution. If the endpoints are not far enough from the specular point, the inversion amplitude is degraded. Cohen (1989) showed empirically that the integration range must increase for deeper reflectors to maintain good amplitudes for parameter estimation.

The major difficulty in estimating parameters was in finding the area under the data filter. The area calculated from the direct arrivals was poor because the source was directional. Most field sources are also directional. For this data set, because the model velocities were known beforehand, the area under the filter could be "determined" by testing several values and choosing the one that gives the best results. With field data, the velocities are not known and this would not work.

3. PSSP SEARCH

This chapter will describe the methods I used to search the Marathon data for possible PSSP wave energy.

I limited the search for PSSP waves to shot records with the shot location, x_s, less than 6000 ft. This is the left side of the model, where the water bottom and next interface are nearly flat. Over the salt dome, where the structure is more complex, the presence of PSSP energy would be difficult to verify because it would be difficult to predict where the PSSP arrivals would occur.

Tatham et al. (1983) describe a method of separating PSSP energy from PP energy in the $\tau-p$ domain. They slant stack a shot record to transform it to the $\tau-p$ domain. (I discuss slant stacking and the $\tau-p$ domain in Appendix A.) Because the water bottom is flat, the incidence angle at the water bottom is equal to the take-off angle. The water velocity is known so they can label the p-axis with the incidence angle. At angles greater than the PP critical angle at the water bottom, no P-waves should penetrate the subsurface, only S-waves. So for p values beyond the critical angle, the only elliptical events the slant stack should show are the water-bottom reflection and PSSP events. In Tatham's slant stack (Figure 3.1), the critical angle is labeled i_c, and the curved events on the right portion of the figure are PSSP reflections. The events labeled A, B, C, and D on the left side of the figure are PP reflections. On the right side, the PSSP reflections from the reflectors corresponding to the labeled PP events are also labeled A, B, C, and D. When inverse slant stacking, Tatham et al. used only the traces with p corresponding to incidence angles between 40 and 75 degrees. The inverse slant stack contained primarily PSSP reflections. With this method, Tatham et al. could easily identify PSSP energy in a shot record and separate it from the PP energy.

I tried to apply Tatham's method to the shot record with $x_s = 2000$ ft (Figure 1.3). I arbitrarily chose this record as one from the section of the model where the first and second interfaces are flattest. The direct arrival and PP reflections from the first three interfaces are the four distinct events, and the PP reflection from the bottom of the model is less distinct at about 1.53 s.

Figure 3.2 is the slant stack of the shot record shown in Figure 1.3. The event in the upper right corner corresponds to the direct arrival. The events on the left edge of the plot correspond to the four PP reflections visible on the shot record. The critical angle occurs at $p = (15750 \text{ ft/s})^{-1} = 63.5 \times 10^{-6}$ s/ft. I will refer to this ray parameter as p_c. To see more events on the slant stack, I applied AGC (Figure 3.3). More curved events are apparent both for p greater than and less than p_c. The curved events are possible partial ellipses from reflections (see Appendix A). Linear events are also more pronounced after gaining; these are edge effects of the slant stack.

Because the PP reflection from the second interface has zero-offset time 1.75 s, a PSSP reflection from that interface must arrive later than 1.75 s. None of the curved

events for $p > p_c$ meet this criterion. For these data, the offsets are not great enough to record reflections beyond the critical angle. Because the water bottom is 2900 ft deep and the maximum offset is 4560 ft, the maximum incidence angle at the water bottom is 38°. The critical angle is 48°. Therefore, there can be no PSSP data recorded beyond the critical angle and I cannot use Tatham's method for identifying or separating the mode-converted energy.

There are, however, some curved events in Figure 3.3 for $p < p_c$ that are not primary PP reflections. These may be PSSP reflections. All these possible PSSP events occur at p greater than 11.8×10^{-6} s/ft whereas only primary PP events occur at p less than 11.8×10^{-6} s/ft. To try to isolate the possible PSSP events, I inverted the slant stack only for p greater than 11.8×10^{-6} s/ft. Because PSSP reflections cannot arrive before PP reflections, I also muted the slant stack for τ less than 0.720 s before inverting it. Figure 3.4 shows the inverse slant stack of Figure 3.3 only for p greater than 11.8×10^{-6} s/ft and τ greater than 0.720 s. The process of slant stacking and inverse slant stacking for specific ray parameters is equivalent to dip filtering. The data in Figure 3.3 have been high-pass dip filtered to create the data of Figure 3.4.

The dip-filtered shot record contains many events that may be PSSP reflections. I analyzed the stacking velocity of these events. Figure 3.5 displays the result of the stacking velocity analysis of Figure 3.4, a contour plot of the semblance across the record after NMO correction has been applied for each of many trial stacking velocities. Peaks in the contour plot indicate strongly hyperbolic events.

I varied the trial stacking velocity from 6000 ft/s to 11500 ft/s. If the stacking velocity of a PSSP reflection were less than 6000 ft/s, the reflection would arrive after the maximum recording time. The maximum possible S-wave interval velocity of the subwater-bottom material is $(15750 \text{ ft/s})/\sqrt{2} = 11140 \text{ ft/s}$. The stacking velocity of a PSSP reflection from the second interface, therefore, should not exceed 11500 ft/s. Because dip is minimal in this portion of the section, I ignore dip effects on the stacking velocity and consider the rms velocity to be the stacking velocity.

The velocity analysis (Figure 3.5) shows one large peak and several smaller peaks which may correspond to PSSP reflections. The large peak occurs at 8500 ft/s and 1.2 s. Smaller peaks occur at 7500 ft/s and 1.35 s, 7700 ft/s and 1.0 s, and 6700 ft/s and 1.75 s. Because the S-wave velocities of the model are unknown, I do not know which of the peaks are in reasonable locations for PSSP events.

Stacking velocity (actually rms velocity) is given by

$$v_s = \left[\frac{\sum_{i=1}^{n} v_i^2 \, t_i}{\sum_{i=1}^{n} t_i} \right]^{1/2} \tag{3.1}$$

(Sengbush, 1983), where t_i is the two-way time through the ith layer and v_i is the interval velocity of the ith layer. Knowing the thickness of both layers and the interval velocity of the water layer allows the stacking velocity and zero-offset time of a PSSP event to be computed for a range of S-wave interval velocities in the second medium. On the contour plot, I have plotted a curve which traces the possible locations of peaks that could correspond to a PSSP reflection from the second interface. A PSSP event must have a peak on or near the curve. Because the large peak at 8500 ft/s and the small peak at 6700 ft/s lie near the curve they may correspond to a PSSP reflection.

Velocity analysis of common shot gathers is not reliable, however. Dip causes the apex of the reflection hyperbola to shift from zero offset. Velocity analysis should be performed on common midpoint gathers where the hyperbola apex is at zero offset regardless of dip. I dip filtered all the shot records for $x_s < 6000$ ft and sorted the data into common midpoint gathers. To improve the signal-to-noise ratio, I stacked five adjacent CMP gathers on offset. Figure 3.6 shows velocity analyses from the stacked CMP gathers centered at $x_m = 1000$ ft to $x_m = 7000$ ft in increments of 1000 ft. The velocity axes (horizontal) range from 6000 ft/s to 11500 ft/s for each of the individual contour plots, and the time axes (vertical) range from 0.6 at the top to 2.0 s at the bottom. The curve plotted on each contour plot is the same curve shown in Figure 3.5. Any possible PSSP event must have a semblance peak on or near this line, and the peak should be present consistently in the individual plots. There are no peaks that consistently fall on the curve in Figure 3.6. There is a consistent peak at 8000 ft/s and 1.2 s on most of the panels. This peak falls near the curve but not on it. I examined the possibility of this peak corresponding to a PSSP reflection.

The dip-filtered data for $x_s < 6000$ ft were stacked with a constant velocity of 8000 ft per second. Figure 3.7 shows the constant velocity stack after AGC has been applied. There is an event at about 1.2 s. The event is nearly flat except near the edges of the plot. A PSSP reflection from the second interface should rise significantly on the right for two reasons. First, the interface is becoming shallower on the right side so the traveltime should decrease. Also, the second layer, through which the S-waves travel, is becoming thinner. The SS leg of the raypath accounts for most of the traveltime because the S-wave velocity is much lower than the water velocity. As the second layer becomes thinner, the traveltime should decrease. The event at 1.2 s is not a PSSP reflection from the second interface. It may be a mis-stacked primary or multiple P-wave reflection.

The Marathon data set does not contain any discernible PSSP reflections above the noise level. The primary reason is the limited maximum offset, as I shall now demonstrate. Brekhovskikh (1980) derives the transmission coefficient for a compressional wave in an acoustic medium converting to a shear wave in an elastic medium:

$$T_{PS} = -\frac{2\,(\rho/\rho_1)\,Z_t \sin 2\gamma_1}{Z_1 \cos^2 2\gamma_1 + Z_t \sin^2 2\gamma_1 + Z}\,, \qquad (3.2)$$

where

$$Z = \frac{\rho c}{\cos \theta} \quad , \qquad Z_1 = \frac{\rho_1 c_1}{\cos \theta_1} \quad , \qquad \text{and} \qquad Z_t = \frac{\rho_1 b_1}{\cos \gamma_1} \quad . \tag{3.3}$$

In equations (3.2) and (3.3), c and c_1 are the compressional velocities in the acoustic and elastic media, respectively, b_1 is the shear velocity in the elastic medium, and θ, θ_1, and γ_1 are the propagation angles of the incident compressional, transmitted compressional, and transmitted shear waves, respectively. The density is ρ in the acoustic medium and ρ_1 in the elastic medium.

Figure 3.8 is a plot of T_{PS} versus incidence angle, θ, for $c = 11750$ ft/s, $c_1 = 15750$ ft/s, and $b_1 = 0.3c_1$. The densities in the acoustic and elastic media are both unity. The notch occurs at the P-wave critical angle. Both peaks increase in amplitude when the shear wave velocity is a greater fraction of the P-wave velocity and the smaller peak increases with respect to the larger one. Clearly, mode conversion is stronger for incidence angles greater than the critical angle.

Brekhovskikh also has the equation for the transmission coefficient for a S-wave in an elastic medium to a P-wave in an acoustic medium. Figure 3.9 is a plot of the S- to P-wave transmission coefficient as a function of the emergence angle of the P-wave. The material parameters are the same as for Figure 3.8. Again, the dominant conversion occurs for incidence/emergence angles greater than the critical angle.

To record significant PSSP energy the offsets must be long enough to record PSSP waves where the P-wave is incident on the water bottom at post-critical angles and the S-wave reflects at the appropriate refraction angle, γ_1. For the Marathon data, assume that the water bottom is a flat plane at depth $z_1 = 2900$ ft and the second interface is a flat plane at depth $z_2 = 4600$ ft. Also assume that the shear wave velocity is 7900 ft/s, or half the compressional wave velocity, in the second layer. The minimum offset to record significant PSSP energy would be

$$(x_r - x_s)_{\min} = 2 z_1 \tan \theta_c + 2 z_2 \tan \gamma_1$$

$$= 8500\text{ft} \quad .$$

This is nearly twice the maximum offset in the Marathon data. The minimum offset required is one third the total length of the model. Such long offsets would make it difficult to image the model with a PSSP survey.

The long offsets required for significant mode conversion and the large recording aperture long offsets require for accuracy of the inversion amplitudes severly limits the usefulness and practicality of PSSP-type marine surveys for both seabed mapping and exploration.

CONCLUSIONS

Common shot, $c(x,z)$, prestack inversion positions the reflectors of the Marathon physical model data set accurately. The inversion parameters may be chosen to image the steep flanks of the shallow dome or the deeper sawteeth better. The wider inversion output better images the steeper reflectors, such as the dome flanks, but the sawteeth have been sacrificed to smile noise. The kinematics of the inversion compare favorably to that of other migrations of the data. Inversion theory provides a means for computing the medium parameters from the inversion amplitudes on reflectors. However, estimating the velocity of progressively deeper layers using the previously estimated velocities causes compounding errors. This was avoided by using the true upper velocity at each interface, and under this constraint, estimates from one shot record inversion gave reasonable values for velocity. Because the model densities are unknown, the validity of the density estimates cannot be verified. The parameter estimation could be improved by using the inversion output from many shot records.

The source-receiver offsets of the Marathon data are not long enough to record reflections incident on the water bottom at angles greater than the critical angle. For this reason, the method used by Tatham et al. for identifying mode converted reflections and separating them from the PP reflections could not be used on the Marathon data. Stacking velocity analysis of dip-filtered CMP gathers from the Marathon data showed one possible peak that may have been the result of a PSSP reflection. Stacking proved that the event could not have been a PSSP reflection because it did not show significant decrease in traveltime towards the center of the model. There is no discernible PSSP energy contained in the data set. The minimum offset required for recording PSSP waves, assuming flat plane reflectors, is 8500 feet. Such long offsets would not allow much of this model to be imaged by PSSP reflections. The potential usefulness of PSSP type marine shear wave surveys, both for exploration and seabed mapping, is limited by the necessarily long offsets. Long offsets require much greater aperture and hence, the ability to accurately estimate parameters will require very long recording arrays and, therefore, entail operational difficulties.

ACKNOWLEDGEMENTS

REFERENCES

Aki, K., and Richards, P. G., 1980, Quantitative seismology, vol. I: W. H. Freeman & Co.

Bleistein, N., 1987, On the imaging of reflectors in the earth: Geophysics, **52**, 931-942.

Bleistein, N., 1984, Mathematical methods for wave phenomena: Academic Press Inc.

Bleistein, N. and Cohen, J. K., 1989, Stacking of narrow aperture common shot inversions: Center for Wave Phenomena Research Report number CWP-080.

Bleistein, N., Cohen, J. K., and Hagin, F. G., 1987, Two and one-half dimensional Born inversion with an arbitrary reference: Geophysics, **52**, 26-36.

Brekhovskikh, L., 1980, Waves in layered media, 2nd edition: Academic Press, Inc.

Brysk, H. and McCowan, D. W., 1986, A slant-stack procedure for point-source data: Geophysics, **51**, 1370-1386.

Cabrera, J. J. and Levy, S., 1984, Stable plane-wave decomposition and spherical-wave reconstruction: Applications to converted S-mode separation and trace interpolation: Geophysics, **49**, 1915-1932.

Claerbout, J. F., 1985, Imaging the earth's interior: Blackwell Scientific Publications, Inc.

Cohen, J. K., 1989, Aperture for Kirchhoff inversion: Center for Wave Phenomena Research Report number CWP-079.

Cohen, J. K., Hagin, F. G., and Bleistein, N., 1986), Three-dimensional Born inversion with an arbitrary reference: Geophysics, **51**, 1552-1558.

Docherty, P. C., 1987, Ray theoretical modeling, migration and inversion in two-and-one-half-dimensional layered acoustic media: Ph.D. thesis, Colorado School of Mines, Golden, Colo. *also* Center for Wave Phenomena Research Report number CWP-051.

Dong, W., 1989, Finite difference ray tracing and common shot inversion: Master's thesis, Colorado School of Mines, Golden, Colo. *also* Center for Wave Phenomena Research Report number CWP-084.

Lighthill, J., 1978, Waves in fluids: Cambridge Univ. Press.

Meissner, R. and Hegazy, M. A., 1981, The ratio of the pp- to the ss-reflection coefficient as a possible future method to estimate oil and gas reservoirs: Geophysical Prospecting, **29**, 533-540.

Neidell, N. S., 1985, Land applications of shear waves: The Leading Edge, **4**, no. 11 32-44.

Neidell, N. S., 1986, Marine applications of shear waves: The Leading Edge, **5**, no. 1, 65-67.

Phinney, R. A., Chowdhury, K. R., and Frazer, L. N., 1981, Transformation and analysis of record sections: J. Geophys. Res., **86**, 359-377.

Robertson, J. D. and Pritchett, W. C., 1985, Direct hydrocarbon detection using comparative P-wave and S-wave seismic sections: Geophysics, **50**, 383-393.

Sengbush, R. L., 1983, Seismic exploration methods: Internat. Human Res. Dev. Corp.

Sullivan, M. F. and Cohen, J. K., 1987, Prestack Kirchhoff inversion of common-offset data: Geophysics, **52**, 745-754.

Tatham, R. H. and Stoffa, P. L., 1976, Vp/Vs--A potential hydrocarbon indicator: Geophysics, **41**, 837-849.

Tatham, R. H., Goolsbee, D. V., Massell, W. F., and Nelson, H. R., 1983, Seismic shear-wave observations in a physical model experiment: Geophysics, **48**, 688-701.

Treitel, S., Gutowski, P. R., and Wagner, D. E., 1982, Plane-wave decomposition of seismograms: Geophysics, **47**, 1375-1401.

Yilmaz, O., 1987, Seismic data processing: Soc. Expl. Geophys.

APPENDIX A

This appendix describes slant stacking, or Radon transform, and the $\tau - p$ domain. Data in the $t - x$ domain, $u(t, x)$, are slant stacked by applying the following operator:

$$\psi(\tau, p) = \int_{-\infty}^{\infty} u(\tau + px, x) dx \qquad (A.1)$$

(Claerbout, 1985). For discretely sampled data, equation (A.1) amounts to summing along lines of constant slope, $p = \dfrac{dt}{dx}$, in the $t - x$ domain for different values of p and τ. τ is the time where the lines, $t = \tau + px$, intercept the time axis. The slope, p, is also the ray parameter $p = \dfrac{\sin\theta}{v}$. This implies that if the surface velocity is known, a slant stack can show the events corresponding to a particular take-off angle.

Straight lines in the $t - x$ domain map to points in the $\tau - p$ domain. The normal moveout (NMO) hyperbola,

$$(tv_{NMO})^2 = x^2 + 4z^2 \quad ,$$

maps to an ellipse,

$$\left(\frac{\tau}{2z}\right)^2 + p^2 = \frac{1}{v_{NMO}^2}$$

(Claerbout, 1985). When p equals zero, τ corresponds to the zero-offset time of the reflection. When τ equals zero, p is the reciprocal of the NMO velocity. Small p corresponds to small take-off angles and flat events in $t - x$. Larger p corresponds to greater take-off angles and steeper events.

An alternative to transforming directly from the $t - x$ to the $\tau - p$ domain, as equation (A.1) does, can be done by to first Fourier transforming the original data (Phinney et al., 1981; Claerbout, 1985). Let the two-dimensional Fourier transform of $u(t, x)$ be $U(k, \omega)$:

$$U(k, \omega) = \int_{0}^{\infty} dt \int_{-\infty}^{\infty} dx \, e^{i(\omega t - kx)} u(t, x) \quad . \qquad (A.2)$$

In the Fourier domain, $p = \dfrac{k}{\omega}$. This is a line passing through the origin. Substituting for k in equation (A.2),

$$U(\omega p, \omega) = \int_0^\infty dt \int_{-\infty}^\infty dx \, e^{i\omega(t-px)} \, u(t, x) \quad . \tag{A.3}$$

Since $t = \tau + px$,

$$U(\omega p, \omega) = \int_0^\infty d\tau \, e^{i\omega\tau} \int_{-\infty}^\infty dx \, u(\tau + px, x) \quad . \tag{A.4}$$

From equation (A.1),

$$U(\omega p, \omega) = \int_0^\infty d\tau \, e^{i\omega\tau} \, \psi(\tau, p) \quad . \tag{A.5}$$

Inverting the Fourier transform of (A.5),

$$\psi(\tau, p) = \frac{1}{2\pi} \int_{-\infty}^\infty d\omega \, e^{-i\omega\tau} \, U(\omega p, \omega)$$

$$= \frac{1}{2\pi} \int_{-\infty}^\infty d\omega \, e^{-i\omega\tau} \int_{-\infty}^\infty dx \, e^{-i\omega px} \int_0^\infty dt \, e^{i\omega t} \, u(t, x) \quad . \tag{A.6}$$

Summarizing, the slant stack can be obtained by two-dimensional Fourier transform of the data, extracting a line of constant p, and inverse temporal Fourier transform of the data along the line. I used this method for all slant stacks in this thesis. The FFT's required padding to a power of two in both time and space. To avoid Fourier wrap-around, I padded with an additional power of two in space.

The inverse of (A.2) is

$$u(x, t) = \frac{1}{4\pi^2} \int_{-\infty}^\infty d\omega \, e^{-i\omega t} \int_{-\infty}^\infty dk \, e^{ikx} \, U(k, \omega) \quad . \tag{A.7}$$

Substituting $k = \omega p$ in (A.7) yields,

$$u(x, t) = \frac{1}{4\pi^2} \int_{-\infty}^\infty d\omega \, |\omega| \, e^{-i\omega t} \int_{-\infty}^\infty dp \, e^{i\omega px} \, U(\omega p, \omega) \quad , \tag{A.8}$$

where $|\omega|$ is the Jacobian of the coordinate transformation. Substituting for $U(\omega p, \omega)$

from (A.5),

$$u(x, t) = \frac{1}{4\pi^2} \int_{-\infty}^{\infty} d\omega \, |\omega| \, e^{-i\omega t} \int_{-\infty}^{\infty} dp \, e^{i\omega p x} \int_{0}^{\infty} d\tau \, e^{i\omega \tau} \psi(\tau, p) \quad . \tag{A.9}$$

This is the inverse of equation (A.6) There are two important differences between (A.9) and (A.6); the exponents in the middle integrals are opposite sign and (A.9) includes $|\omega|$ whereas (A.6) does not.

By changing the order of integration in (A.9) and applying the convolution and shift theorems, an inverse of the form of equation (A.1) is obtained:

$$u(x, t) = \frac{1}{2\pi} \rho(t) * \int_{-\infty}^{\infty} \psi(t - px, p) \, dp \quad . \tag{A.10}$$

In equation (A.10), the asterisk means convolution and $\rho(t)$ (known as the *rho filter*) is the inverse Fourier transform of $|\omega|$.

Because of the similarities of (A.9) and (A.6) I could use the same program for inverse slant stack as for forward slant stack. Next, the rho filter must be applied. $|\omega|$ can be factored as $[-i\omega] \cdot [i \, \mathrm{sgn}(\omega)]$. Since $i \, \mathrm{sgn}(\omega)$ is the Fourier transform of the Hilbert transform kernel, $\frac{1}{\pi t}$,

$$\rho(t) * f(t) = \frac{d}{dt} H\{f(t)\} \quad , \tag{A.11}$$

where $H\{f(t)\}$ is the Hilbert transform of $f(t)$. I applied the rho filter by Hilbert transforming the data and the multiplying it by $-i\omega$ in the frequency domain.

As mentioned earlier, a slant stack can show the events corresponding to a particular take-off angle. In other words, a slant stack decomposes a wave field to plane waves. This is only true, however, for line-source data. A slant stack of point source data is kinematically a plane-wave decomposition. The amplitudes of the slant stack are not correct for plane-wave decomposition though (Yilmaz, 1987). Several authors consider plane-wave decomposition for point-source data if the medium possesses radial symmetry. (Brysk and McCowan, 1986; Cabrera and Levy, 1984; Treitel et al., 1982). The amplitude treatment in point-source, plane-wave decomposition is unnecessary unless one is concerned with the amplitudes in $\tau-p$ space. A forward and inverse slant stack, if done properly, should give the correct amplitudes in the $t-x$ domain.

Marathon Data Model

Distance x (Feet)

$V_p=11750$ ft/s

$V_p=15750$ ft/s

$V_p=22410$ ft/s

$V_p=15750$ ft/s

$V_p=19900$ ft/s

Depth z (Feet)
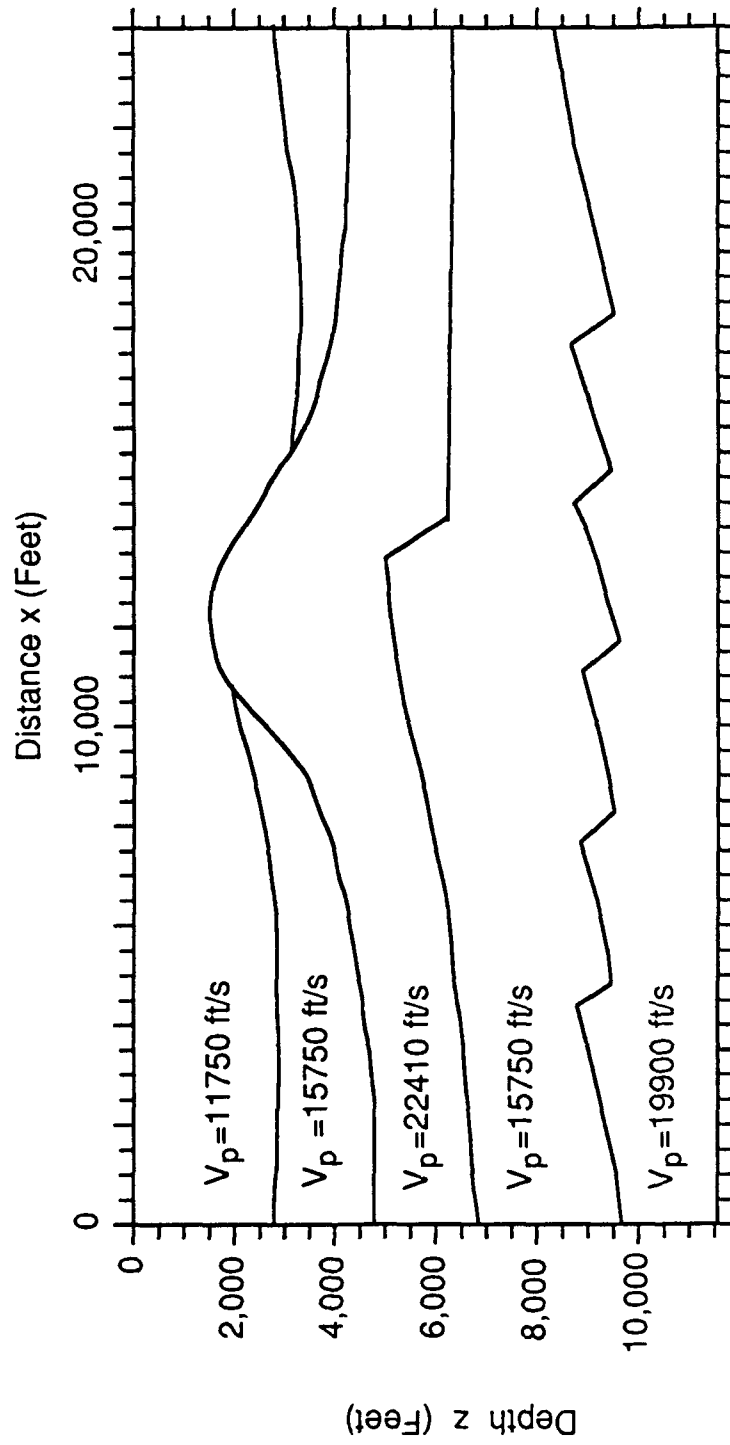
Figure 1.1:   Cross section of data model.

Marathon Data Recording Geometry

Source

48 Receivers

800 ft

80 ft

4560 ft
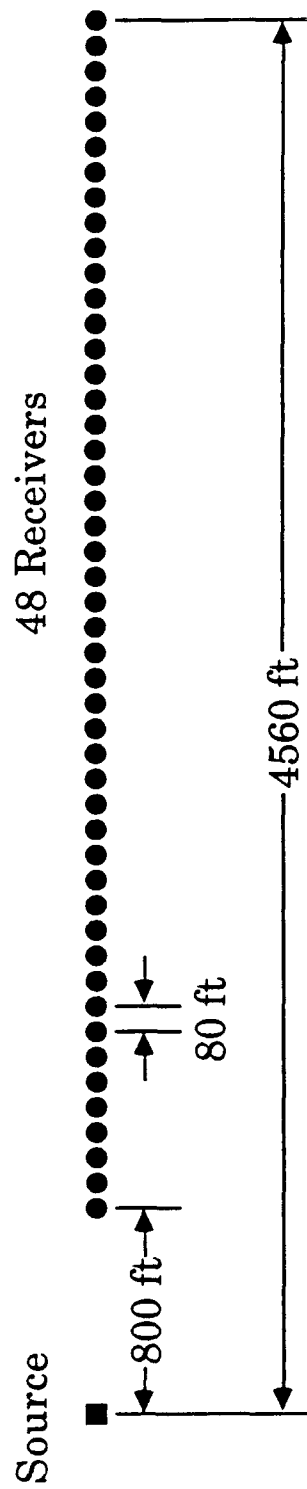
Source move-up = 80 ft

290 Shots

Figure 1.2:   Schematic of recording array for each shot in data.

Shot 2000
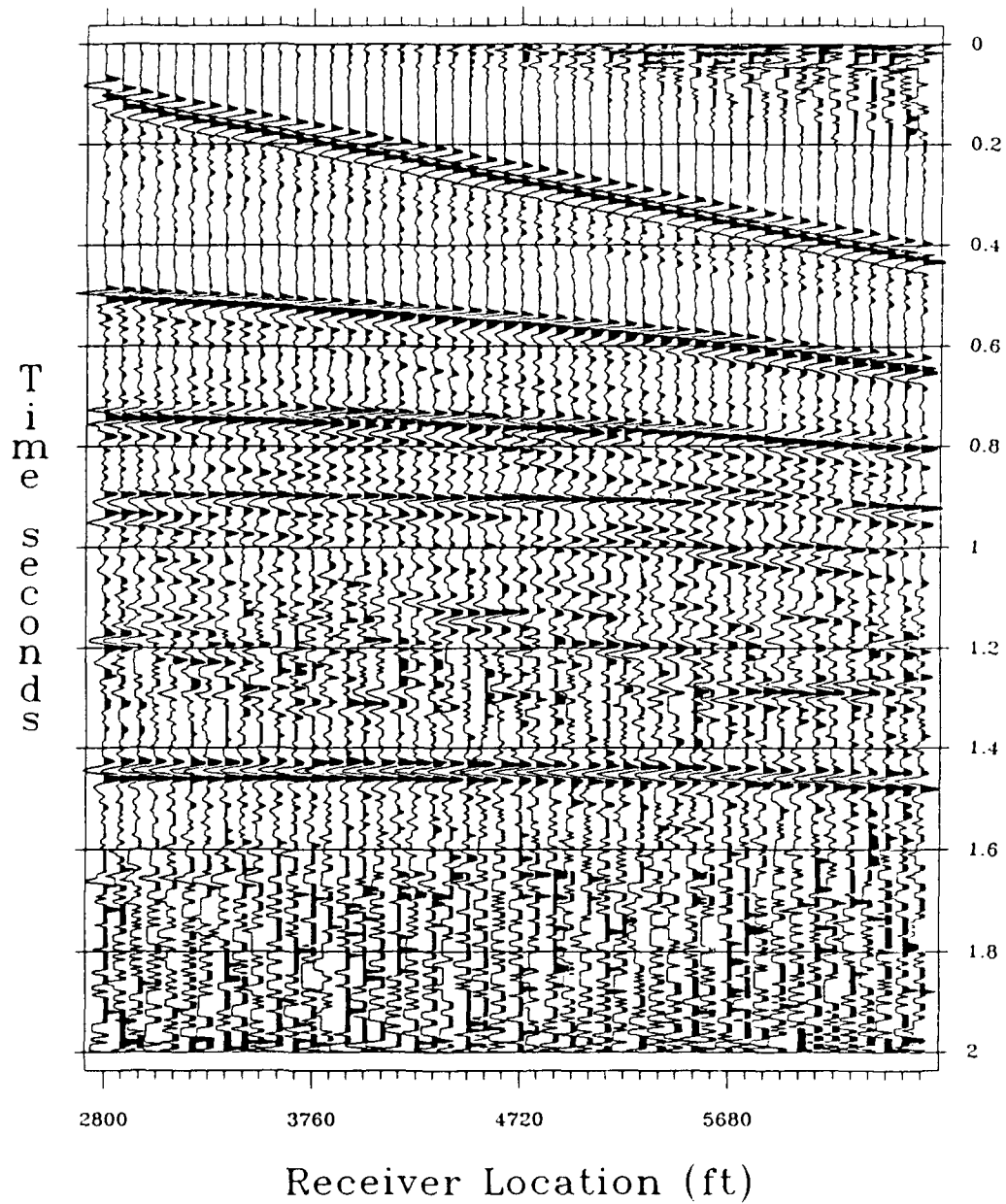
Figure 1.3: Sample shot record from the Marathon data. AGC with a 200-sample (0.8 s) window has been applied.

PSSP   Geometry
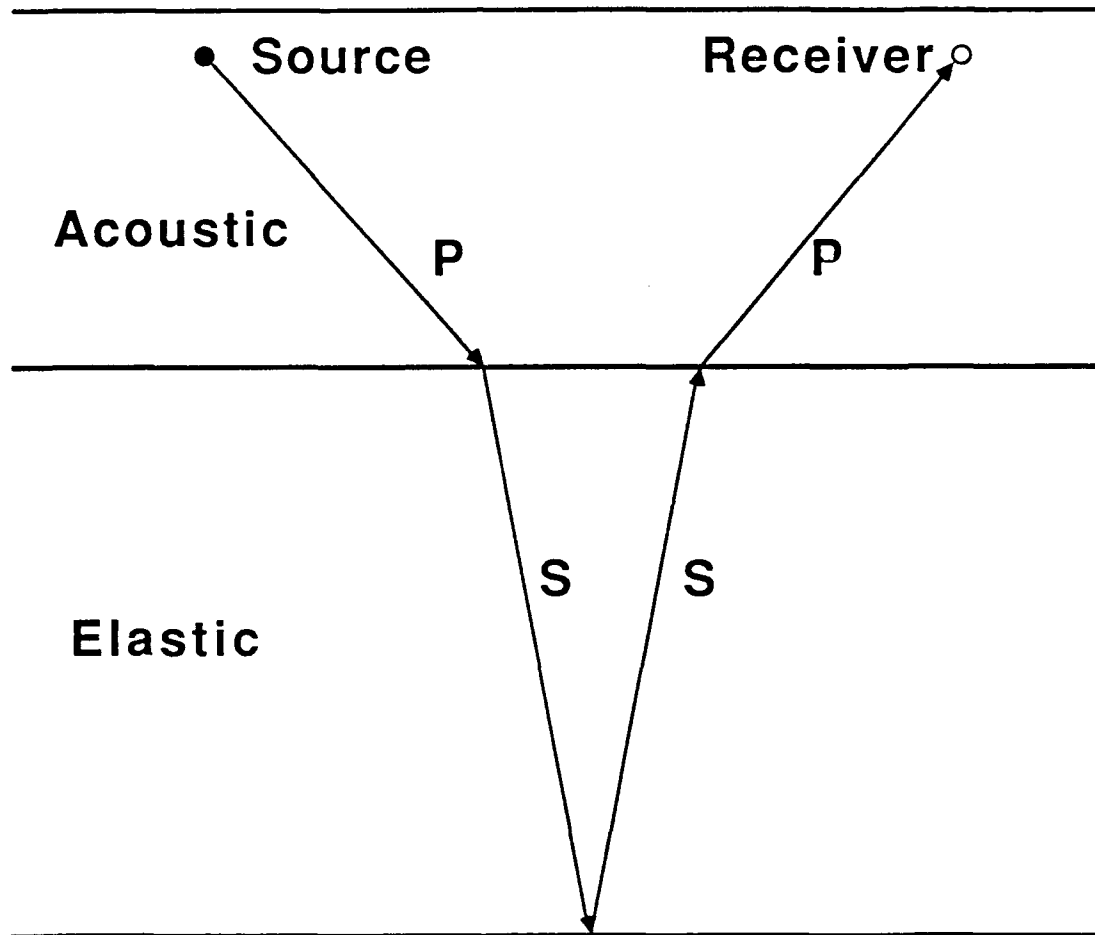
Figure 1.4:   Ray paths follow by PSSP mode converted waves.

First Background Model

Distance (ft)
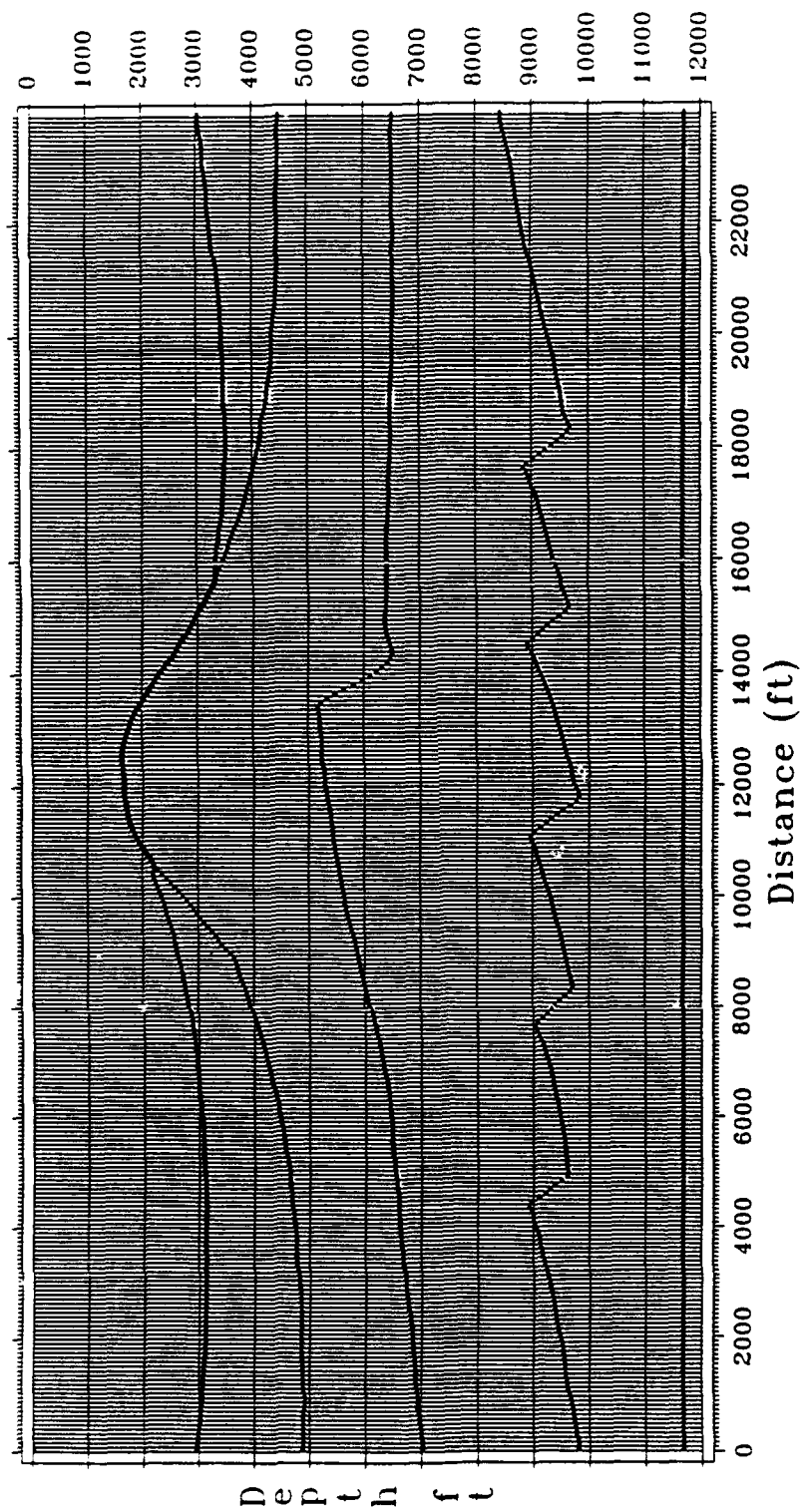
Figure 2.1: The interfaces of the constant velocity layers of the background velocity function for the first inversion.

Inversion of Shot 2000
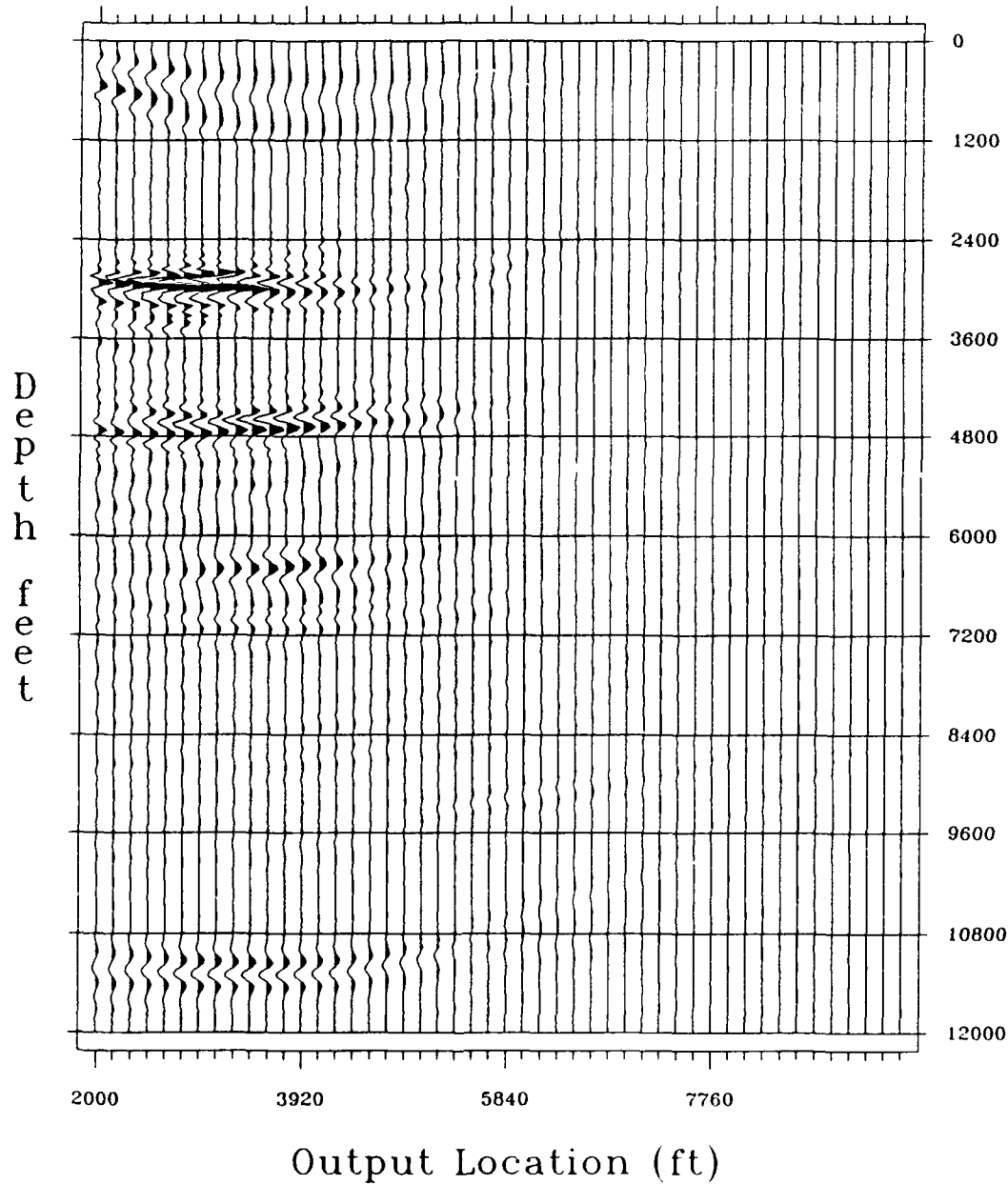
Figure 2.2: Inversion of the shot record in Figure 1.3. Inversion is applied to the ungained record. The inversion shows partial images of the reflectors.

Stack of All Shot Inversions
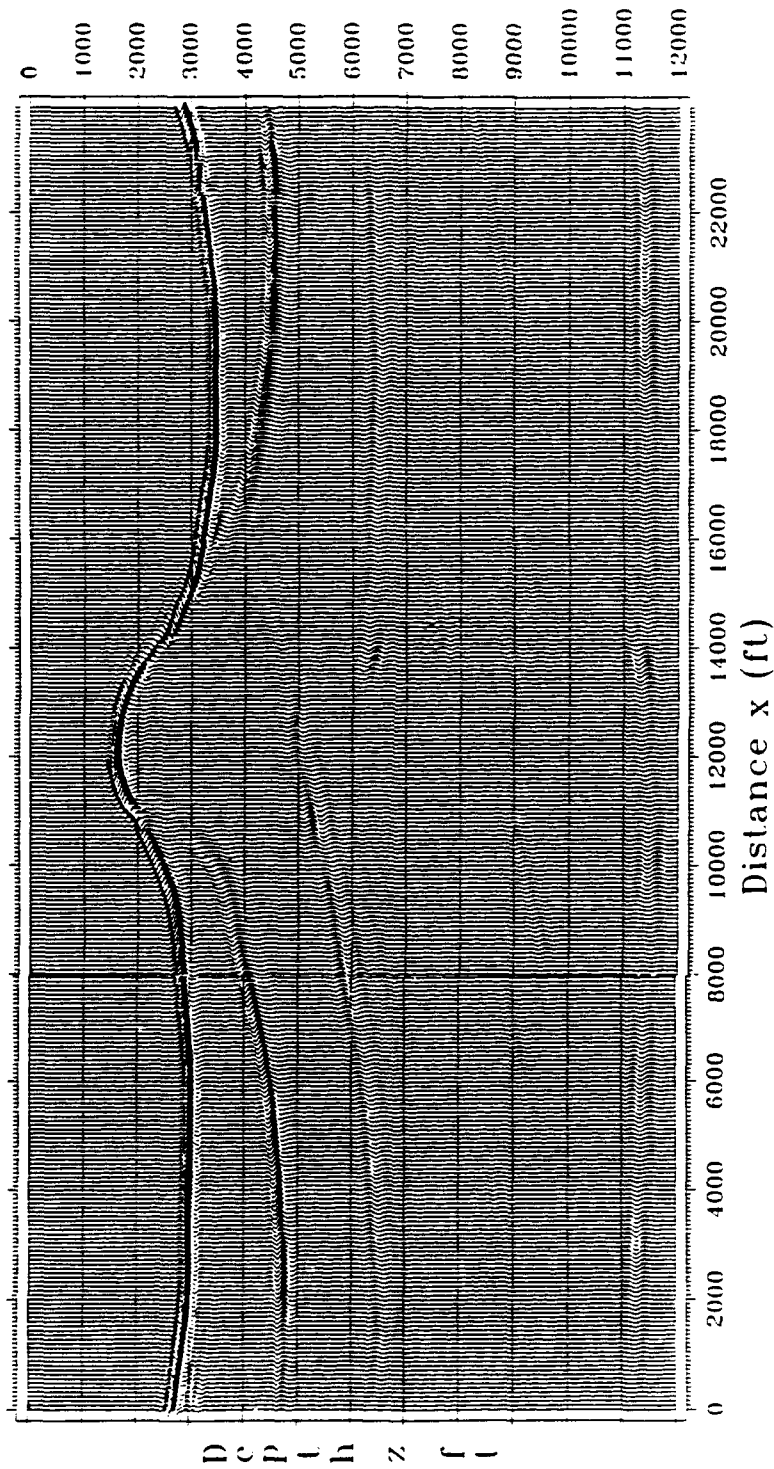
Figure 2.3: Stack of inversions of all shot records. The reflectors are completely imaged, but the sawtooth reflector is hard to see.
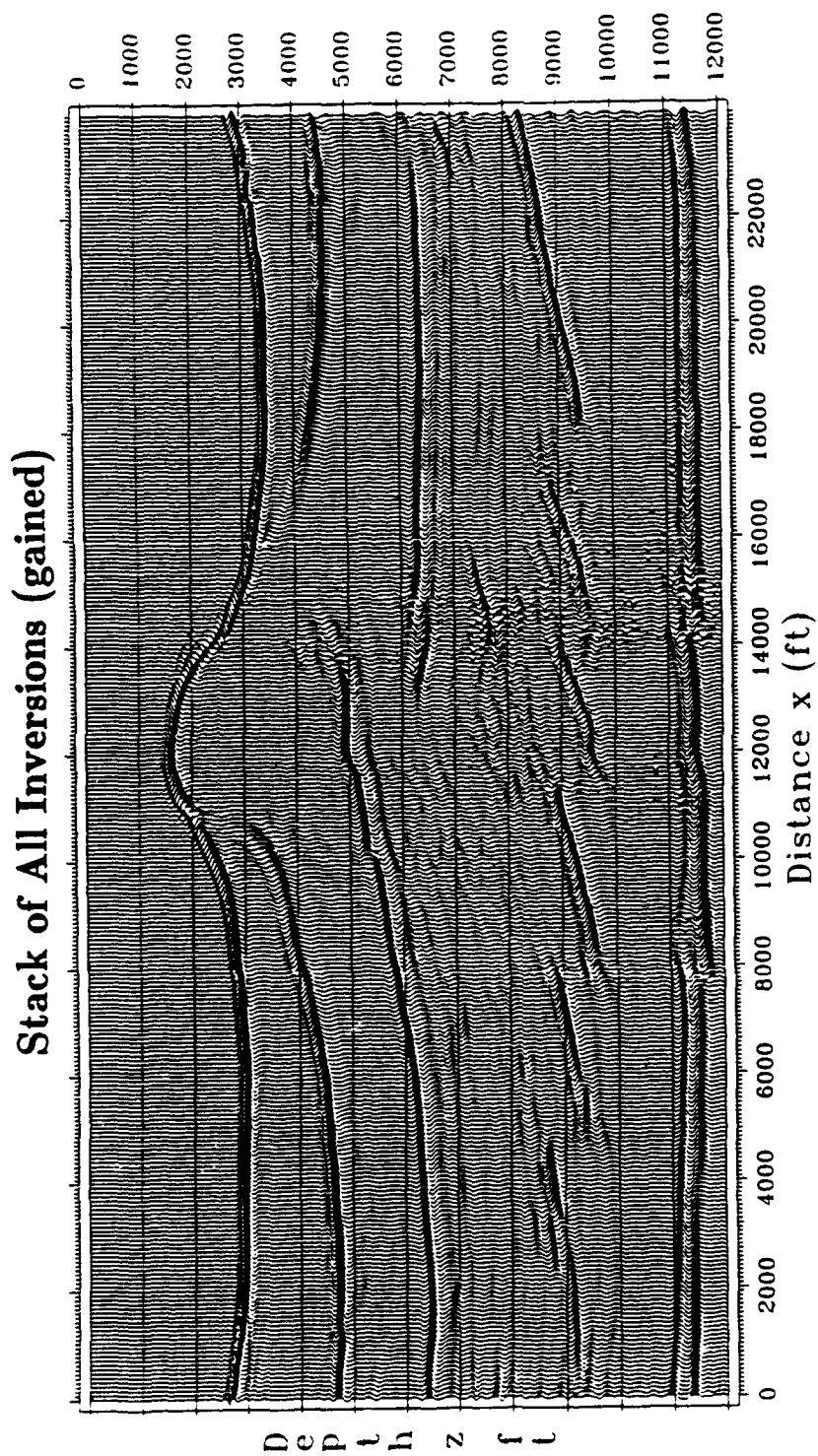
Figure 2.4: Stacked section of Figure 2.3 after applying AGC with a 200-sample (8000 feet) window.

Reflection Ellipse
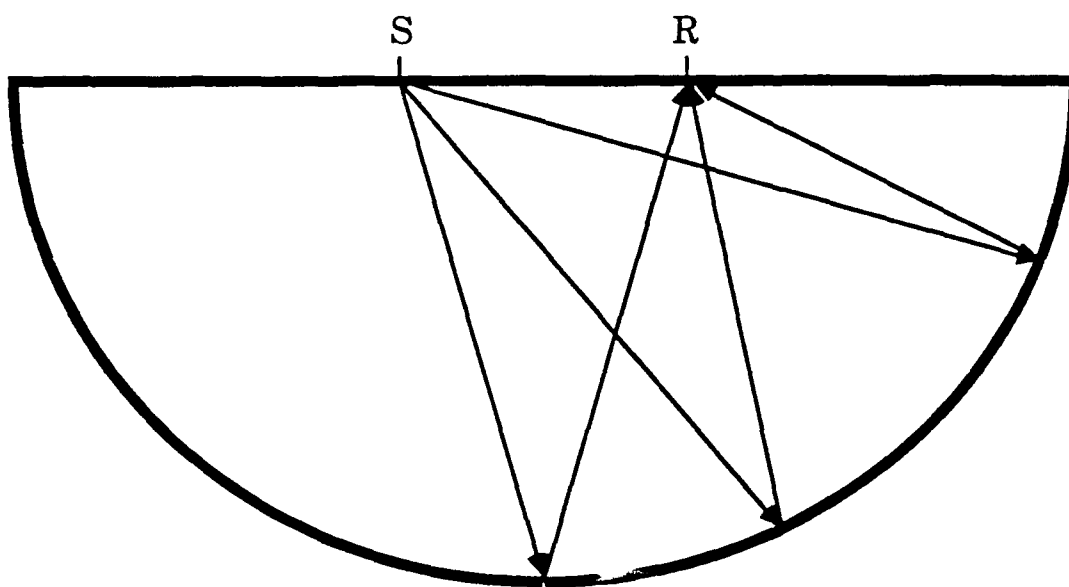
Figure 2.5: The envelope of all reflectors having the same reflection time. It is an ellipse with the source and receiver at the foci. Steep reflectors would be farther than flat reflectors from the source-receiver midpoint.
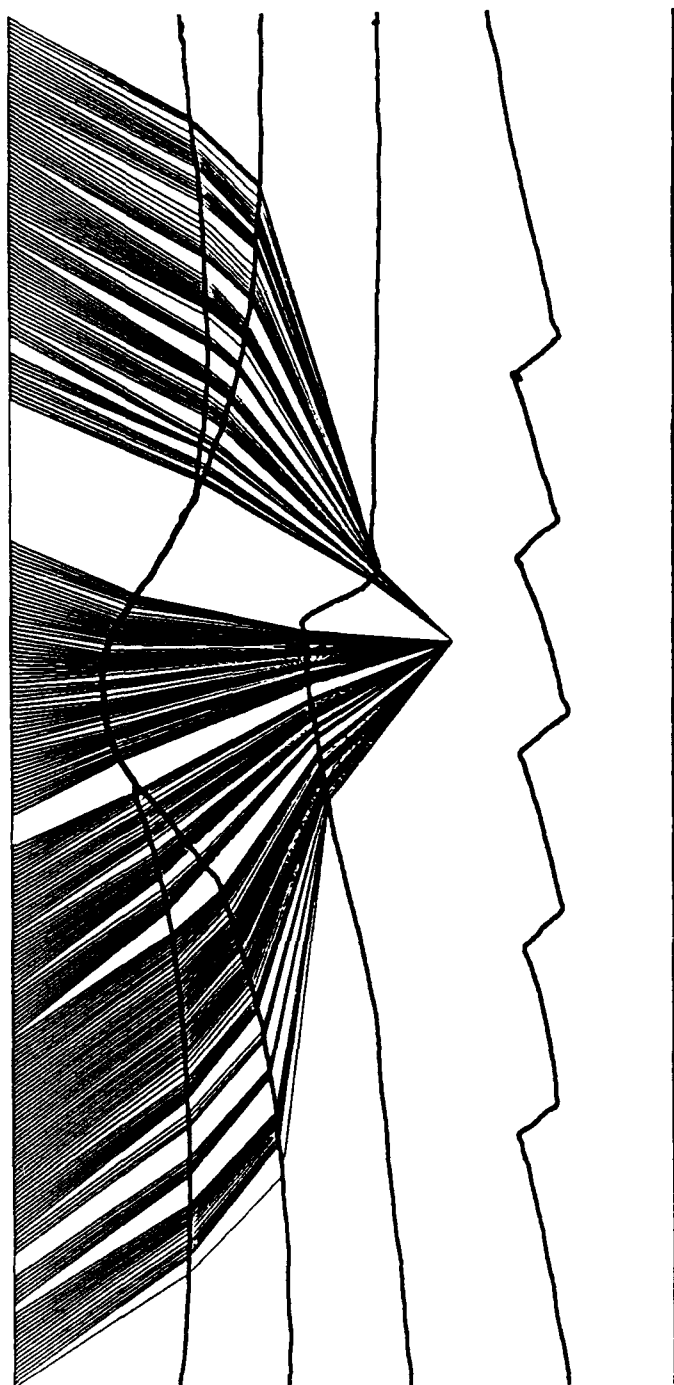
Figure 2.6: Ray tracing from a subsurface point ($z = 13000$ feet, $z = 7800$ feet) to equally spaced points on the surface using the first background velocity function.

Second Background Model
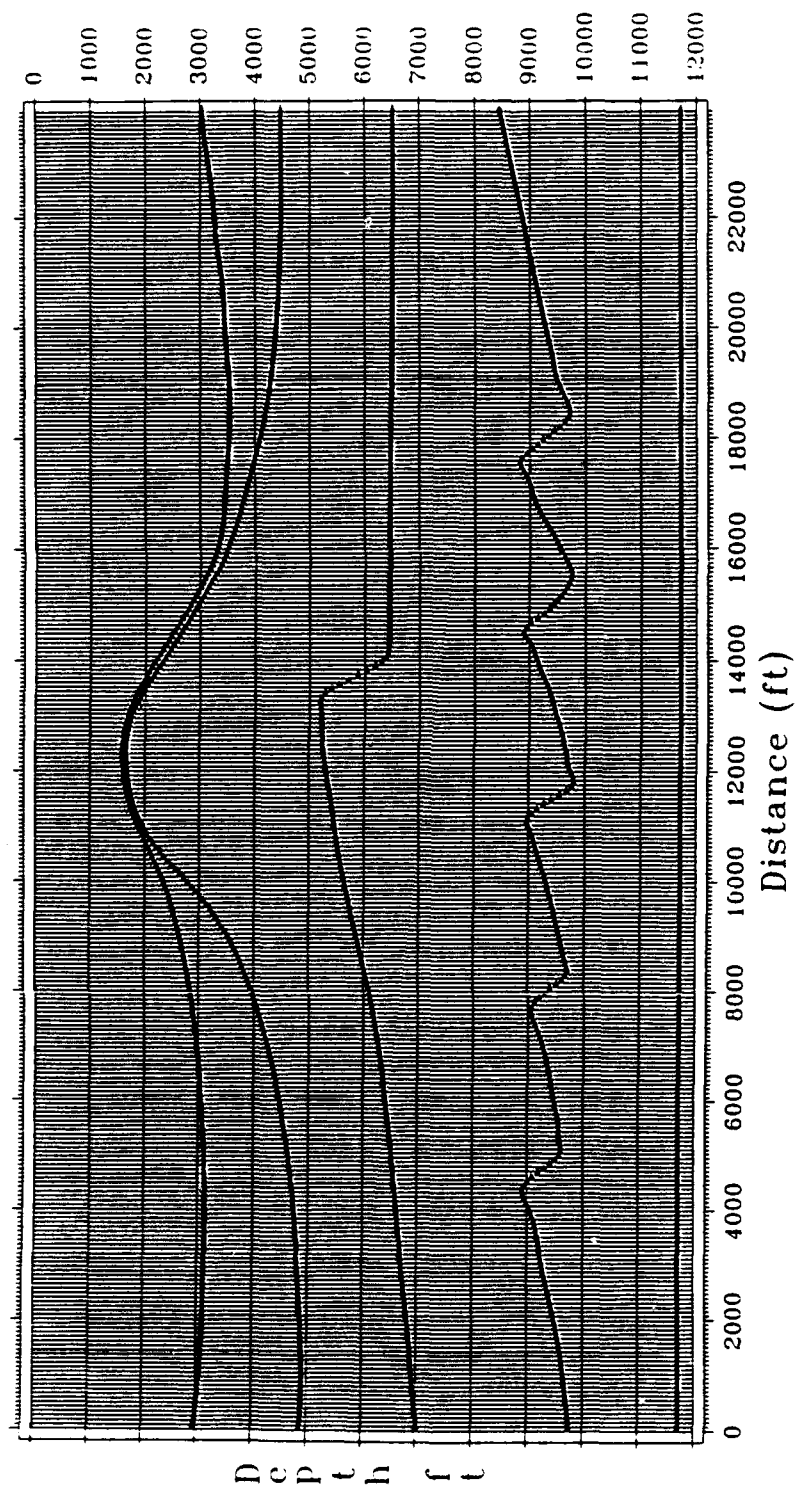
Figure 2.7: The smoothed interfaces of the constant velocity layers of the background velocity function for the second inversion.
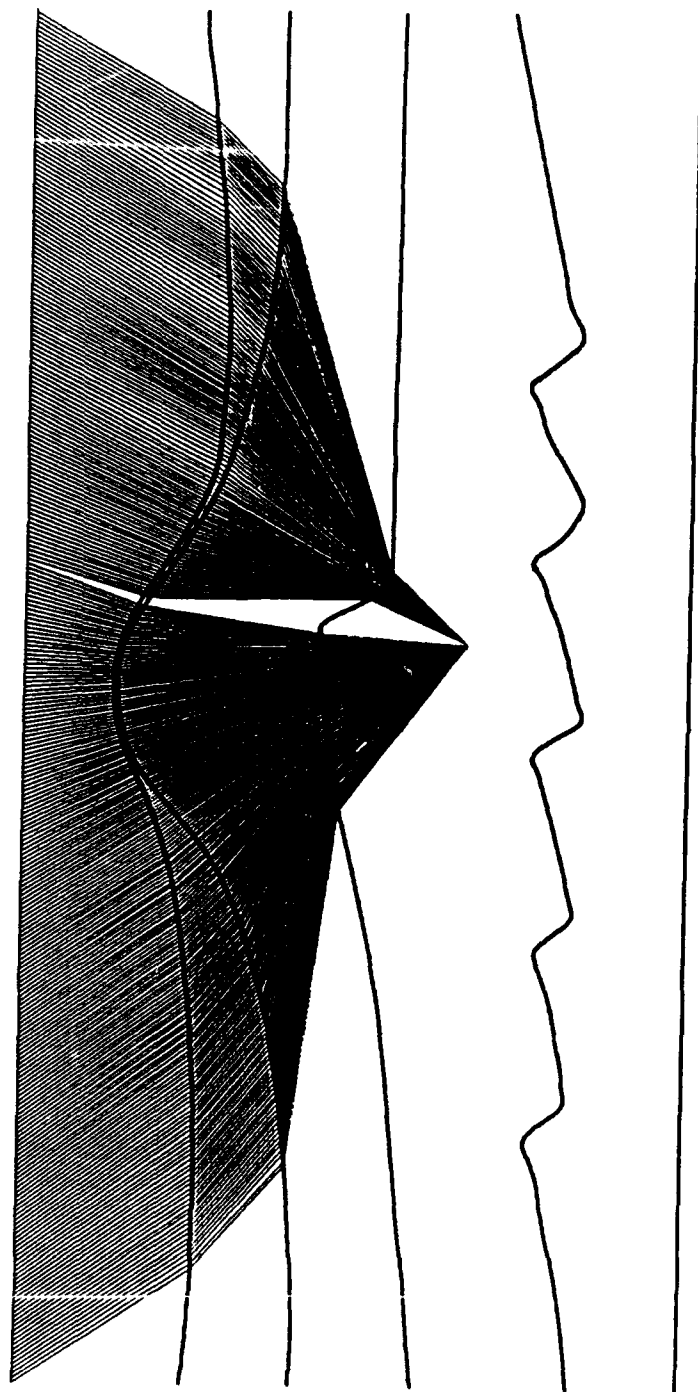
Figure 2.8: Ray tracing from a subsurface point ($x = 13000$ feet, $z = 7800$ feet) to equally spaced points on the surface using the second background velocity function.

Inversion of Shot Record
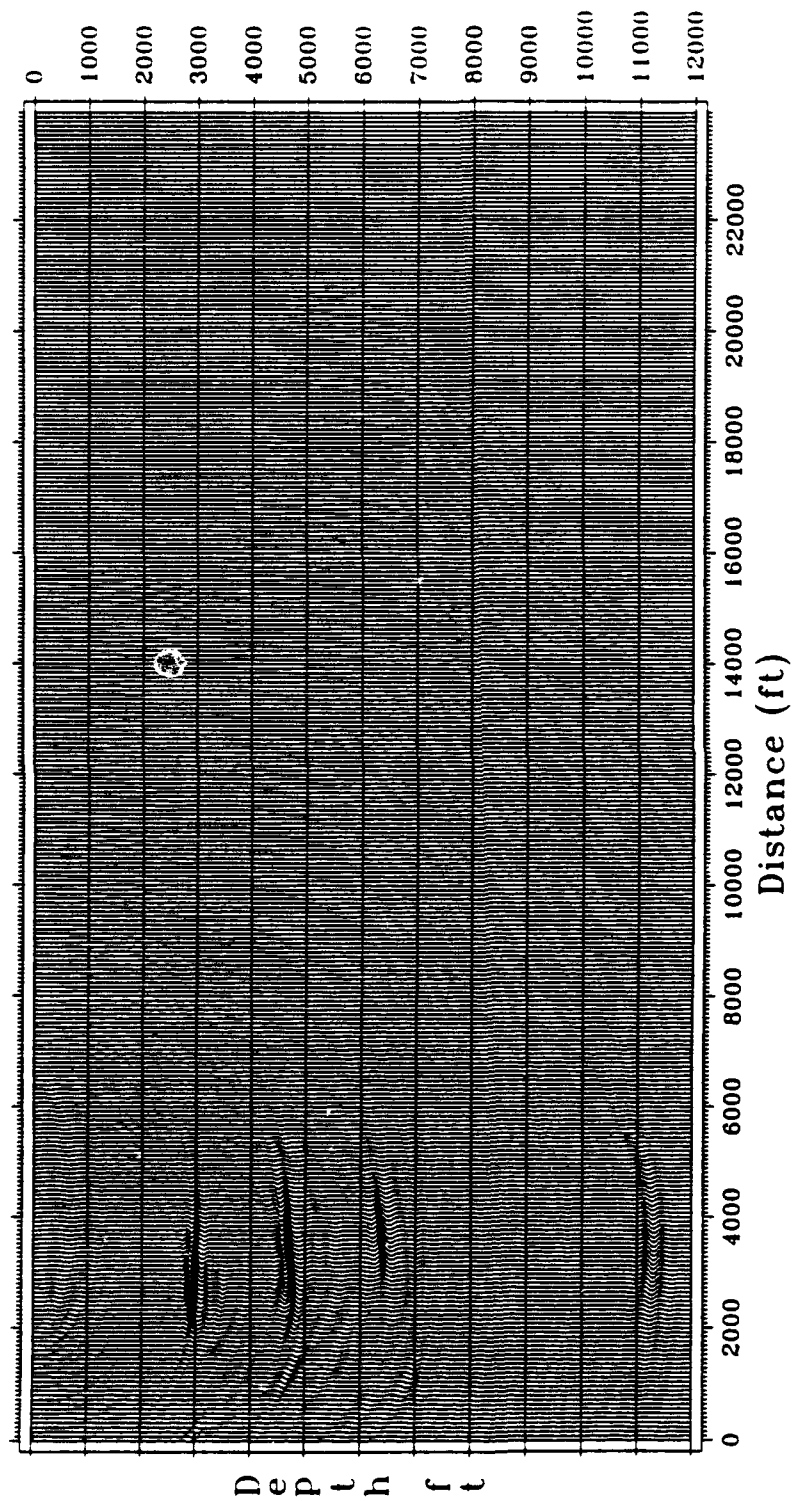
Figure 2.9: Second inversion of the shot record shown in Figure 1.3. The impulse response smiles cover a greater portion of the inversion than the images.

Stack of All Shot Inversions (gained)
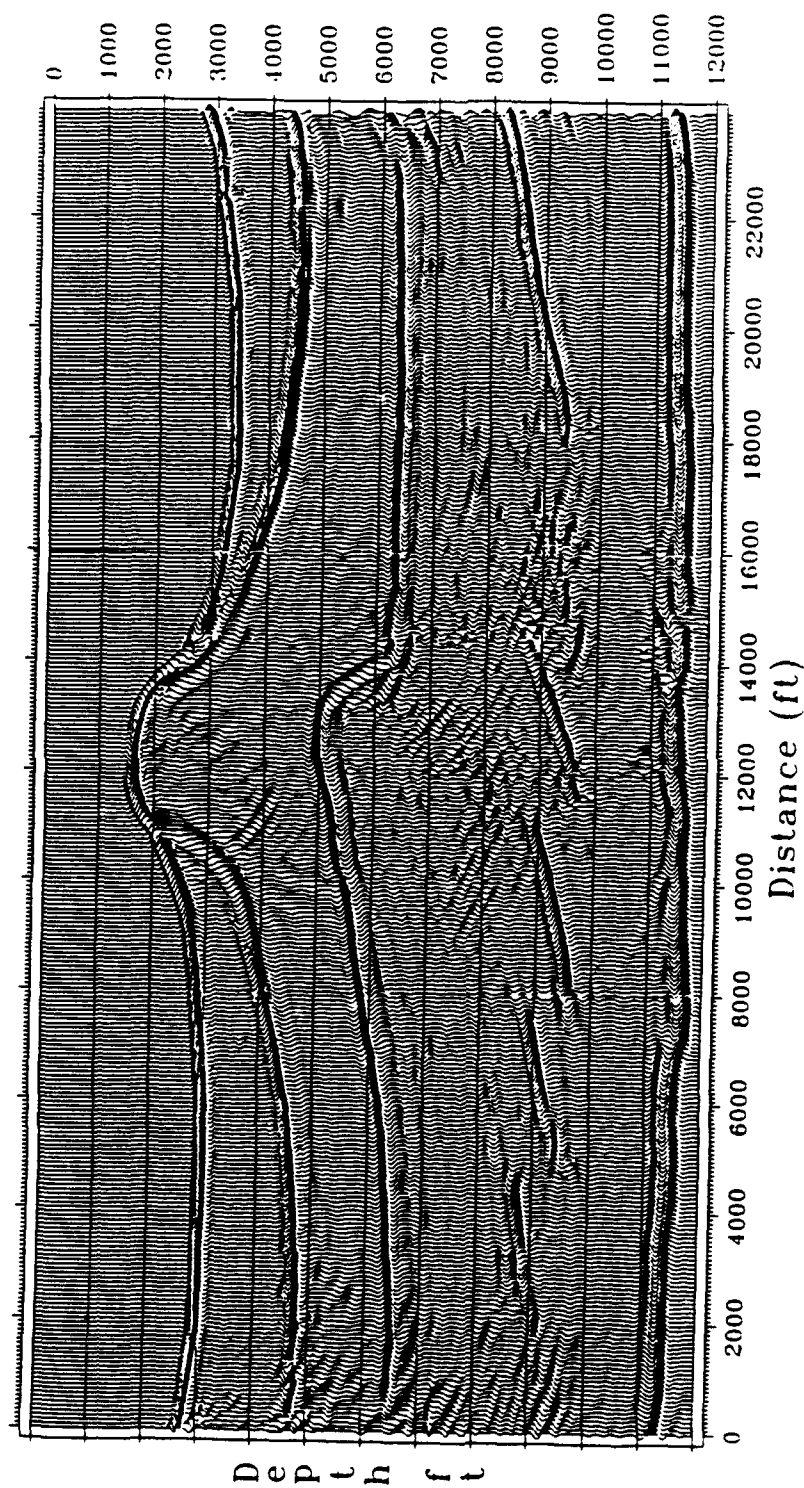
Figure 2.10: Stack of second shot inversions after AGC. Steeper events and the third interface fault plane have been imaged better than in Figure 2.4 but there is more smile noise.
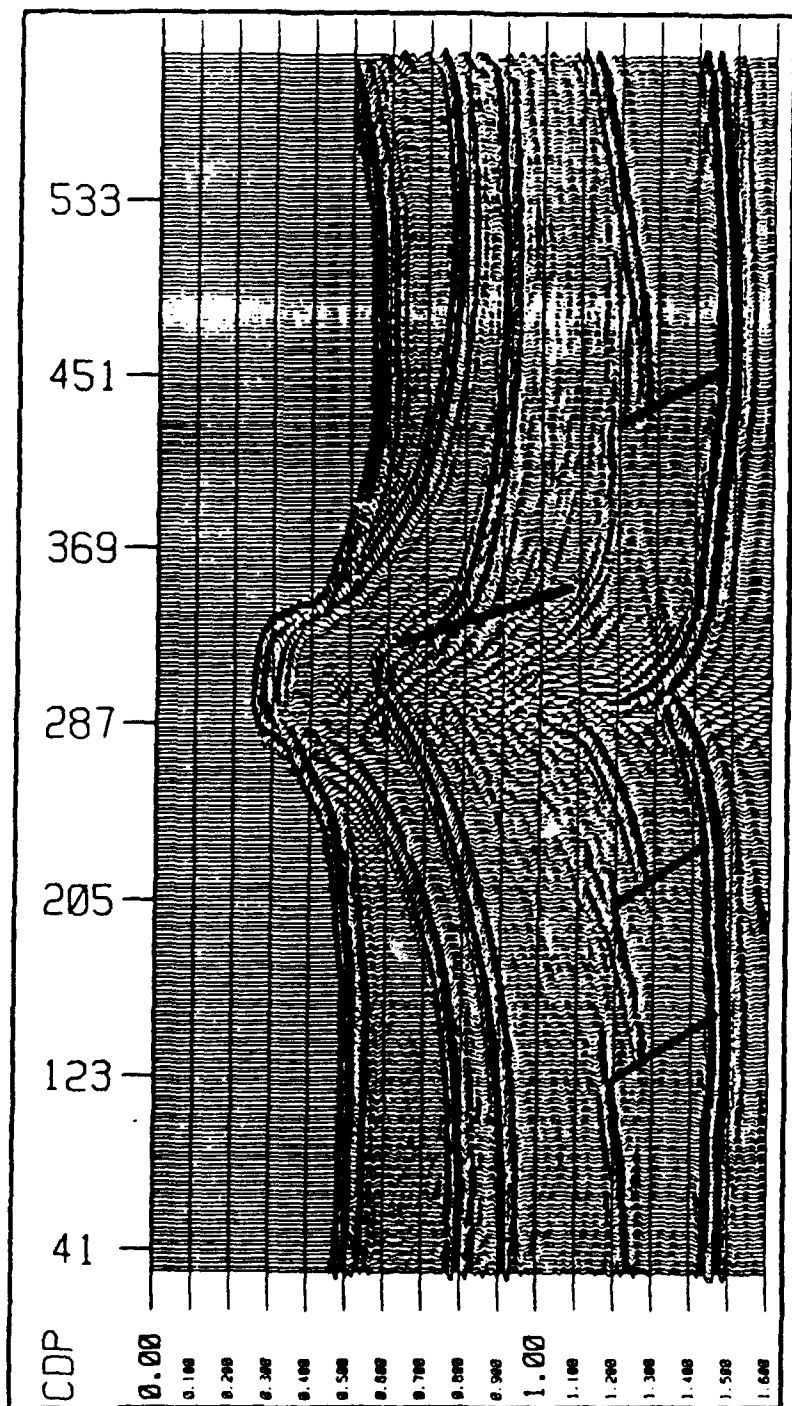
TIME MIGRATION

(FINITE DIFFERENCE METHOD)

Figure 2.11: Finite-difference, time migration by the University of Houston. The fourth and fifth sawteeth are not imaged.
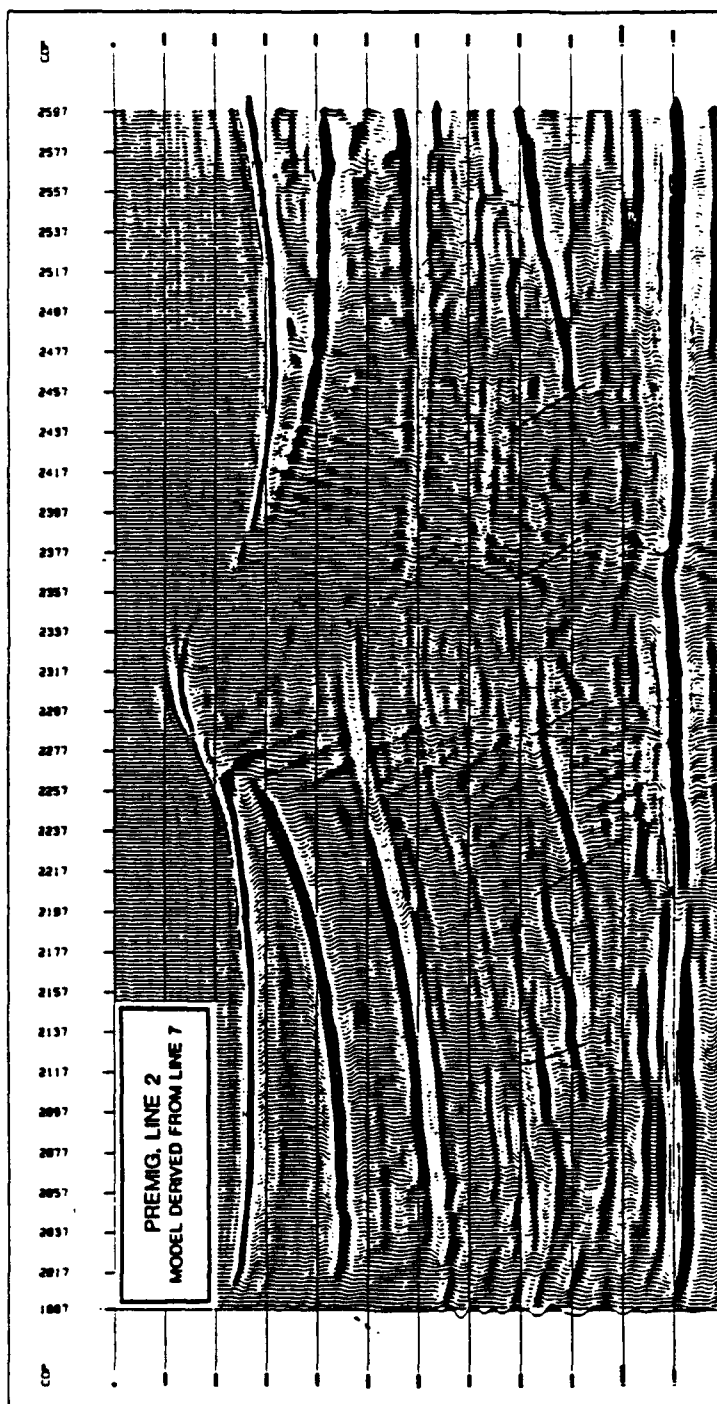
Figure 2.12: Prestack, finite-difference, depth migration by Marathon Oil Company. The fifth sawtooth is absent.

Inversion of Shot 2000
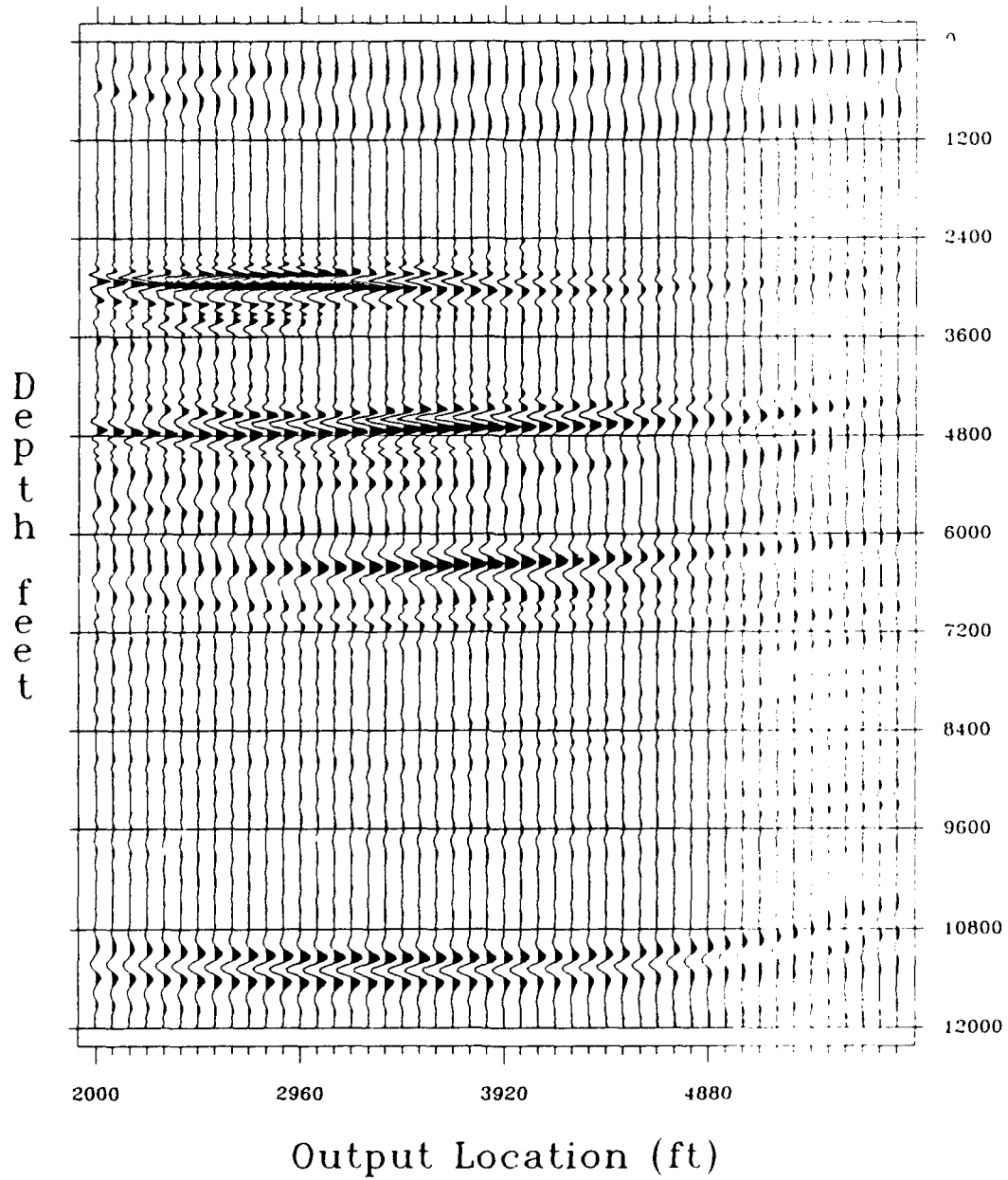
Figure 2.13: Inversion (β) of the shot record in Figure 1.3 for parameter estimation.
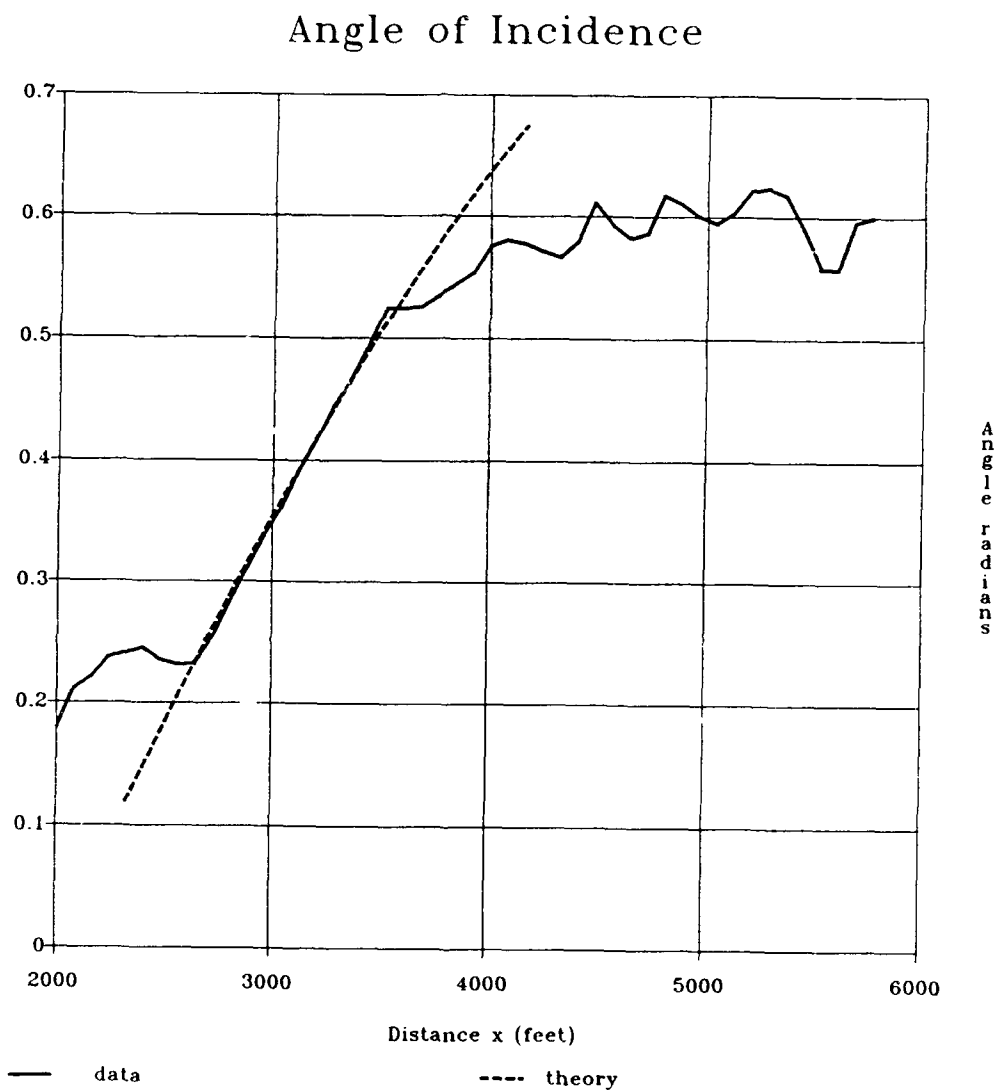
Angle of Incidence

Figure 2.14: Angle of incidence of rays at the first interface. The solid line is the inverse cosine of the ratio of β to β_1. The dashed line is $\tan^{-1}(x/5400)$, the theoretical angle if the first reflector is a flat plane a $z = 2700$ feet.

Estimating Velocity and Density
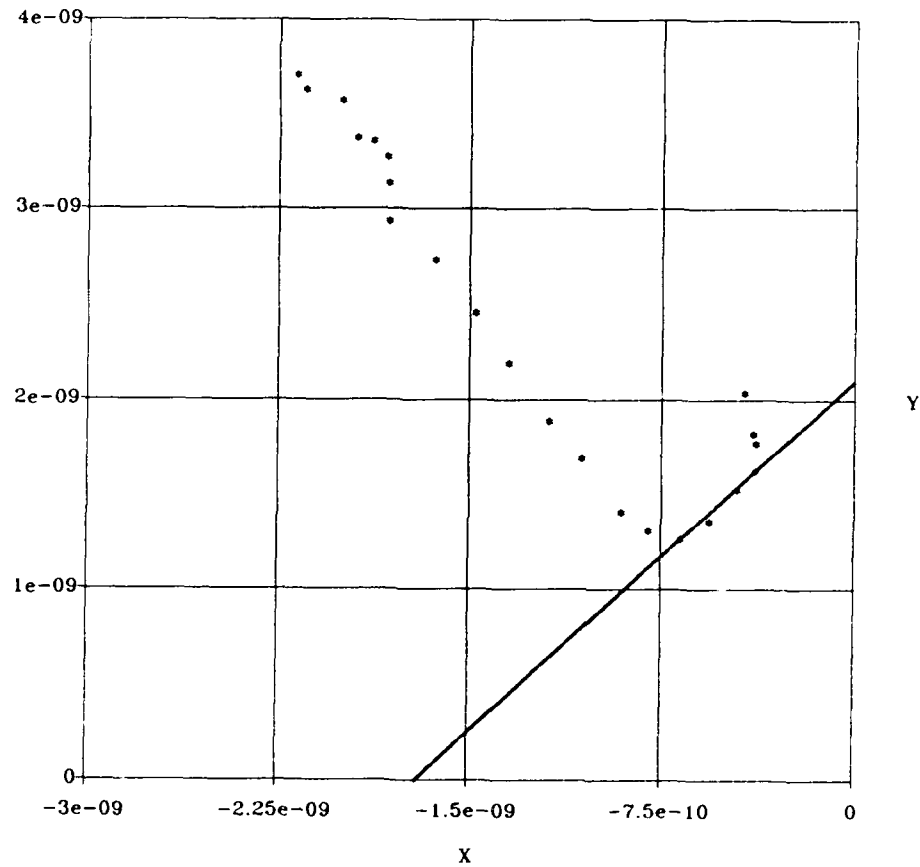
Figure 2.15: Plot for estimating velocity and density from the inversion
amplitudes of the first reflector. $X = -\sin^2\theta/c^2$ and,
$Y = (1-R)^2/(1+R)^2 \times \cos^2\theta/\rho^2 c^2$. The slope of the best fit line is
the reciprocal of the square of the density. The X-intercept is the
reciprocal of the square of the velocity.
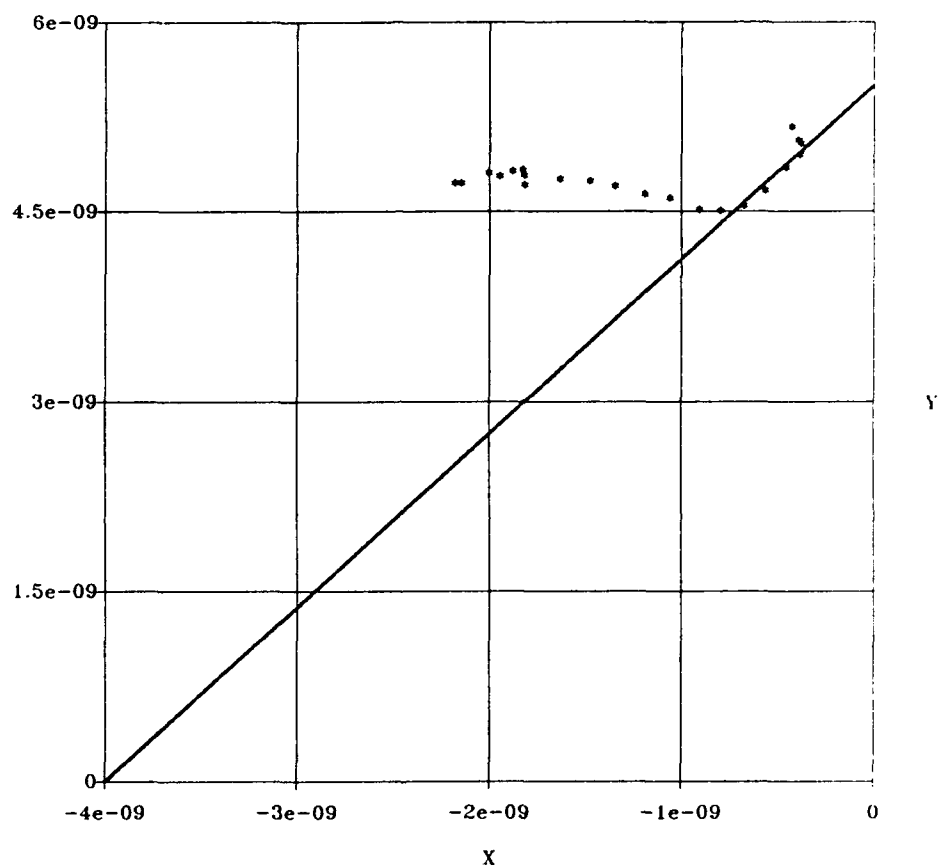
Estimating Velocity and Density

Figure 2.16: Plot for estimating velocity and density from the inversion amplitudes with the area under the filter selected so that the velocity is 15750 feet/s.
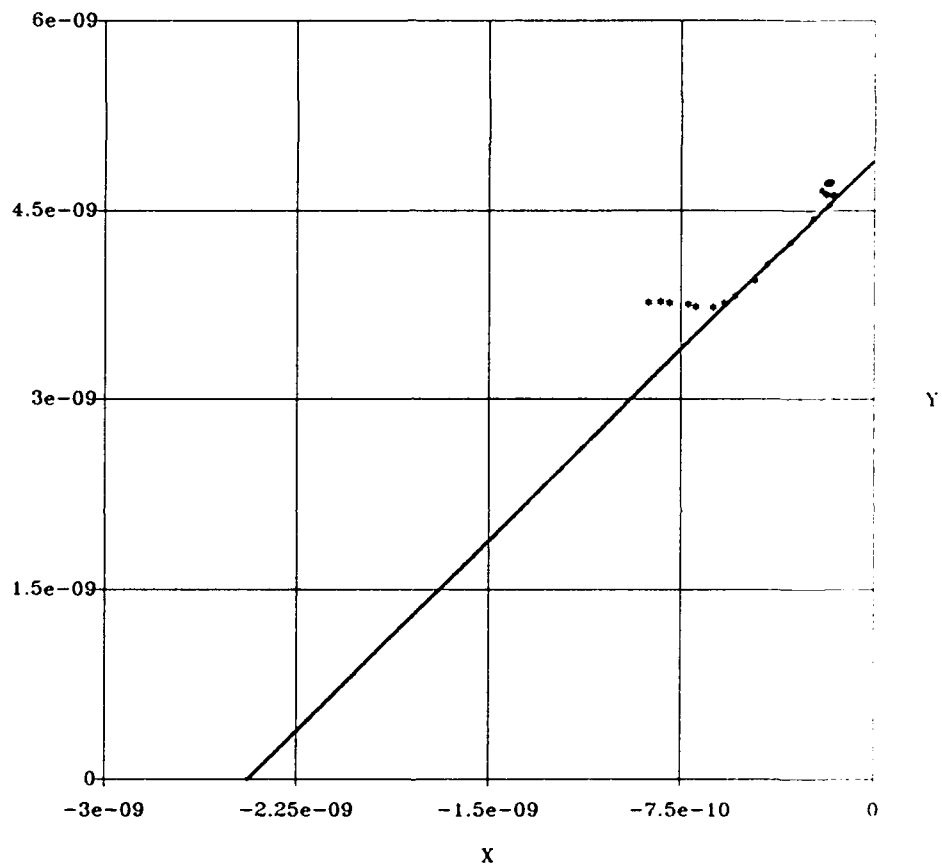
Estimating Velocity and Density

Figure 2.17: Plot for estimating velocity and density from the inversion amplitudes of the second reflector.
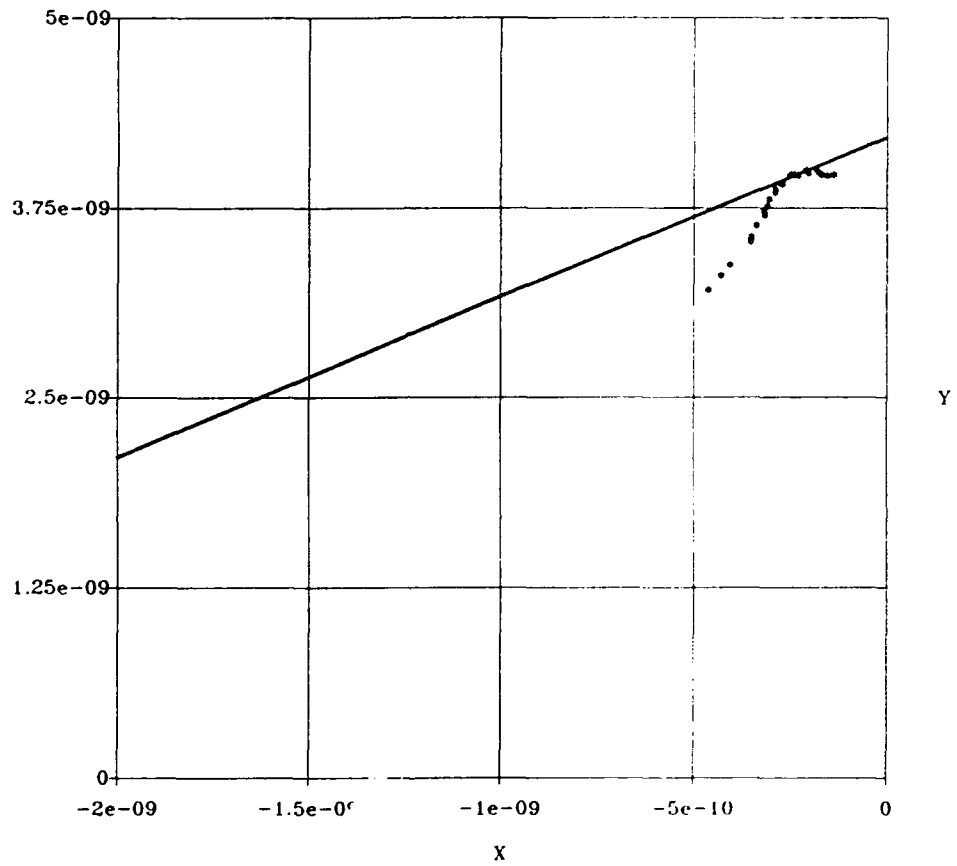
Estimating Velocity and Density

Figure 2.18: Plot for estimating velocity and density from the inversion amplitudes of the third reflector.
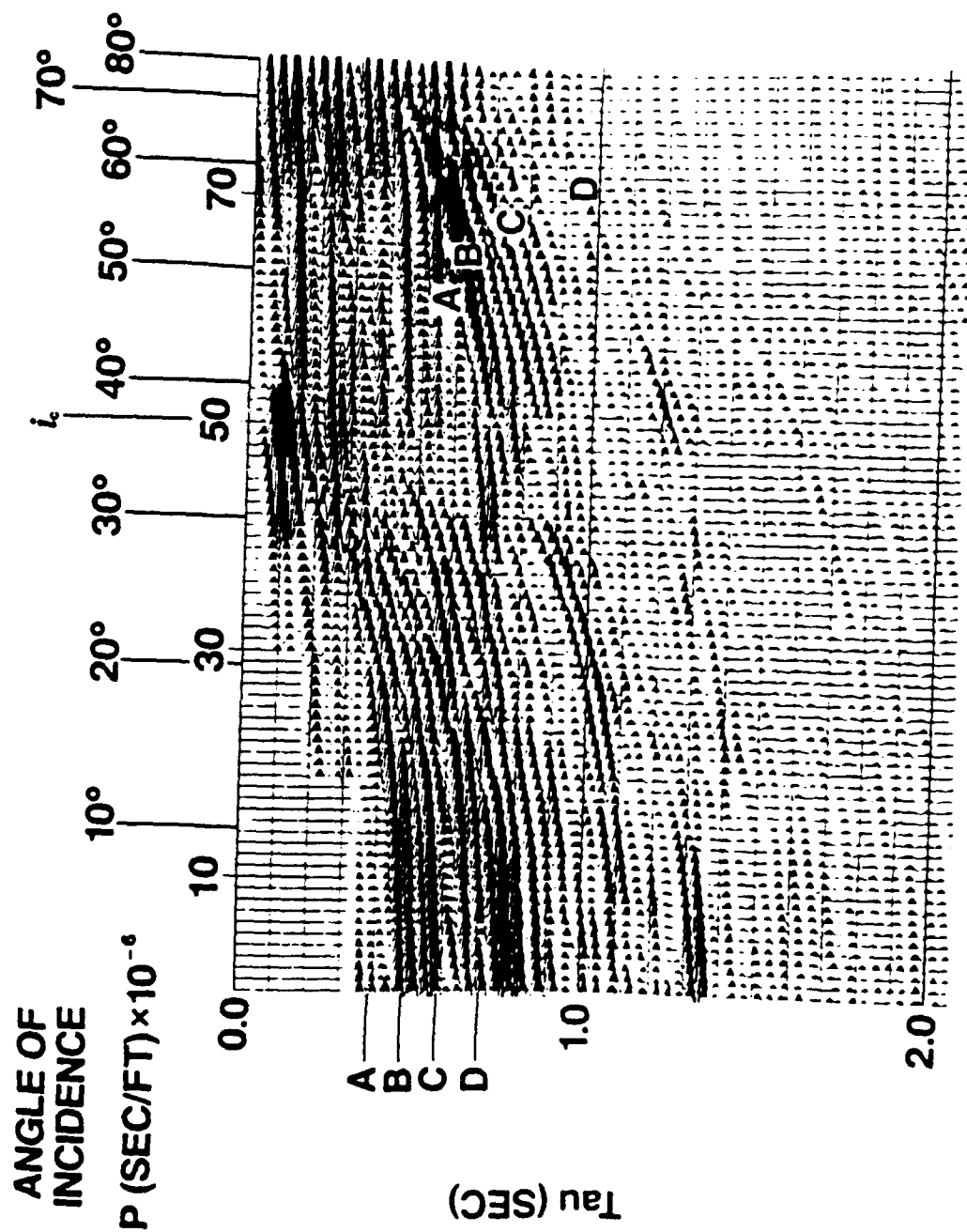
Figure 3.1: Slant stack of physical model shot record from Tatham et al. (1983).
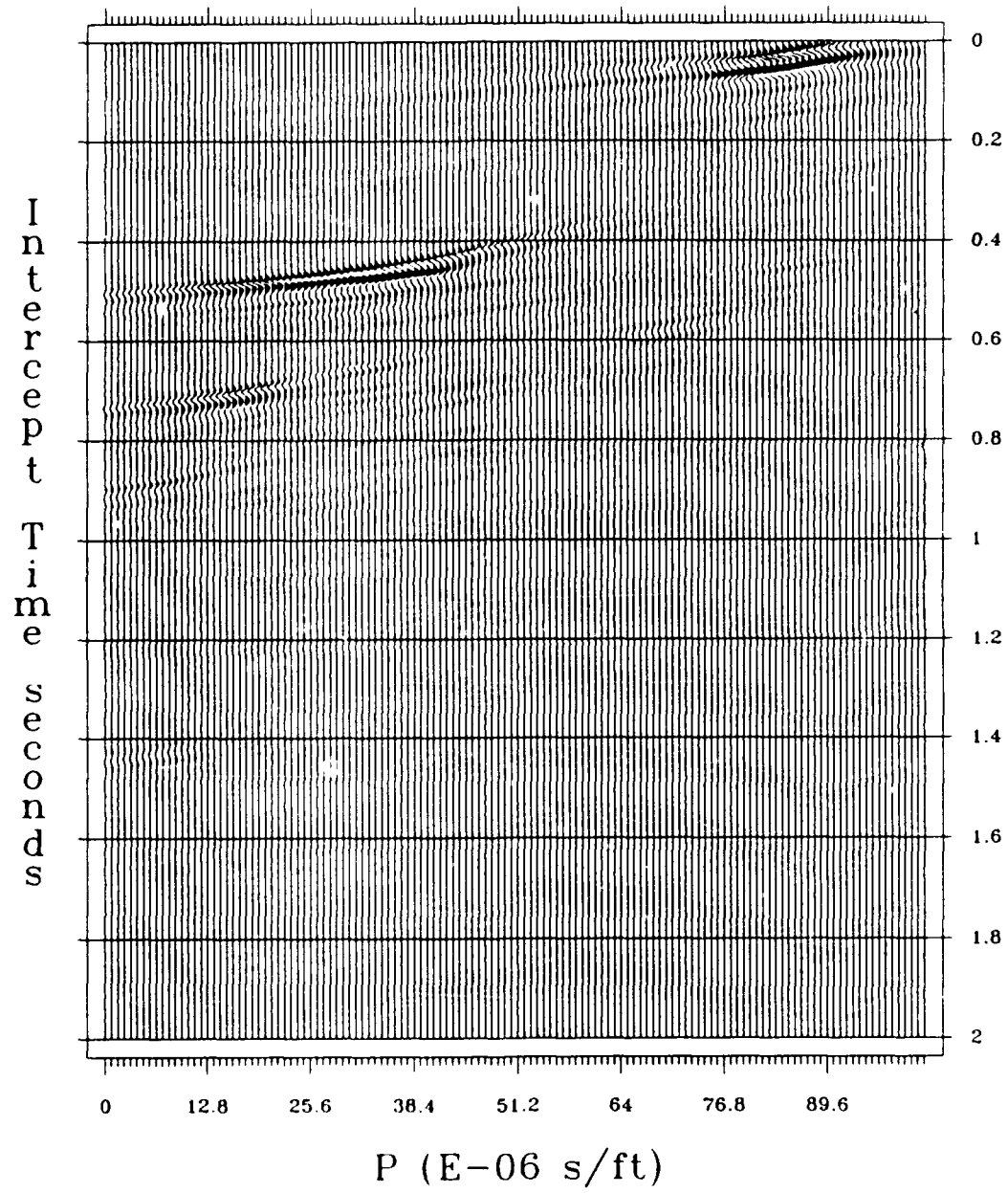
Slant Stack of Shot 2000

Figure 3.2: Slant stack of the (ungained) shot record shown in Figure 1.3.
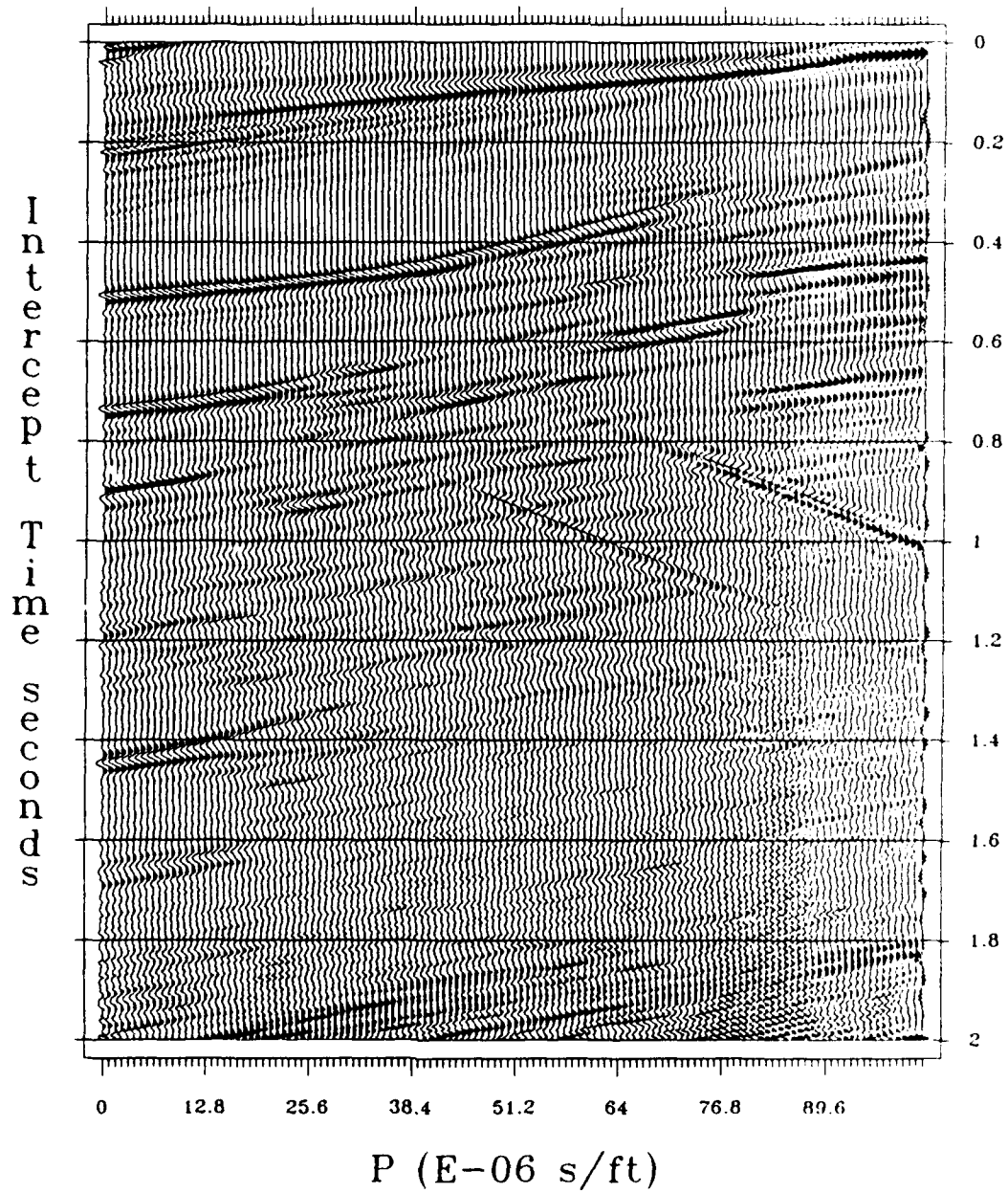
Slant Stack of Shot 2000 (agc)

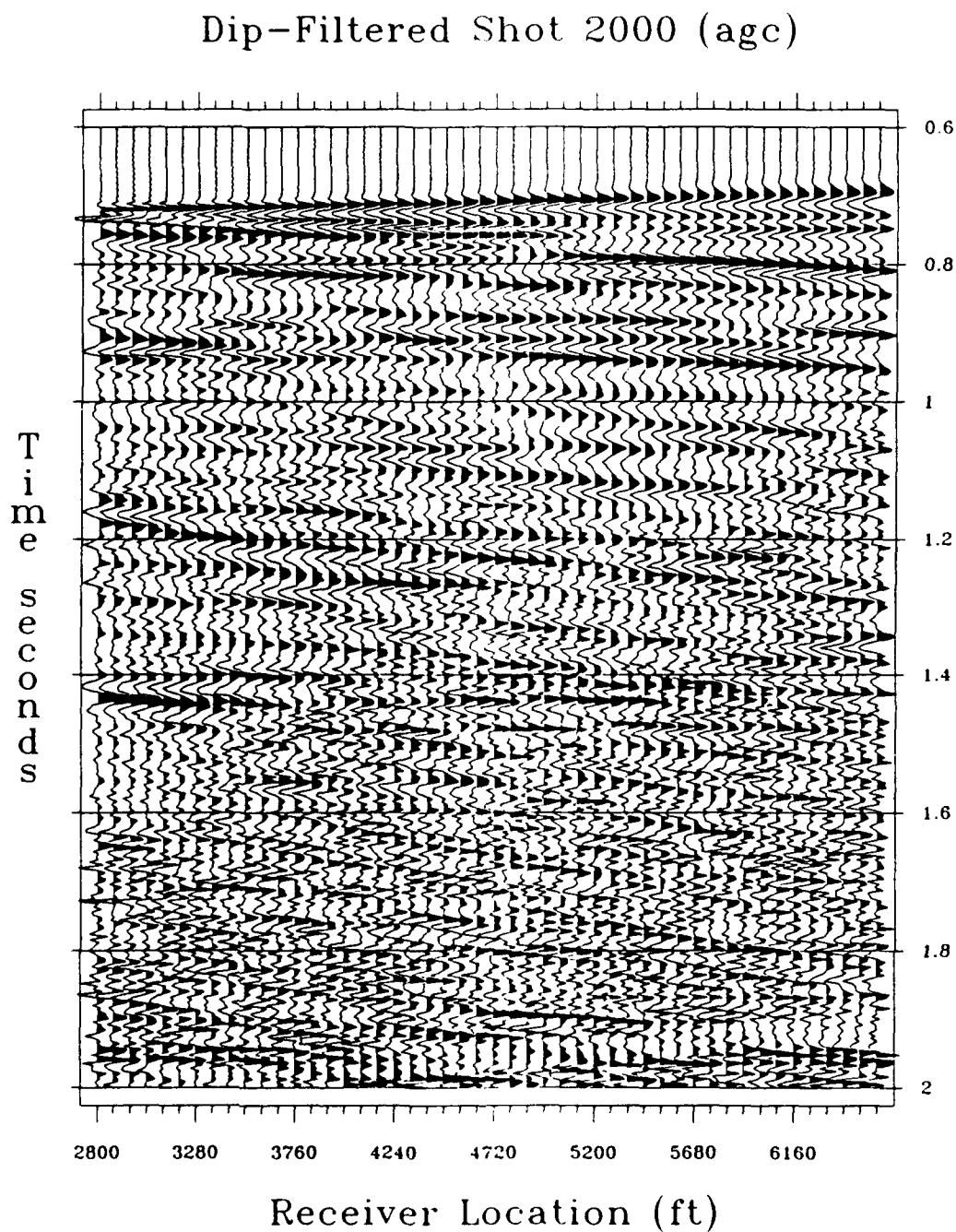Figure 3.3: Slant stack in Figure 3.2 after AGC with a 200-sample (0.8 s) window.

Figure 3.4: Inverse slant stack of Figure 3.2 for $p > 11.8 \times 10^{-6}$ s/ft. This is the shot record in Figure 1.3 after dip filtering.
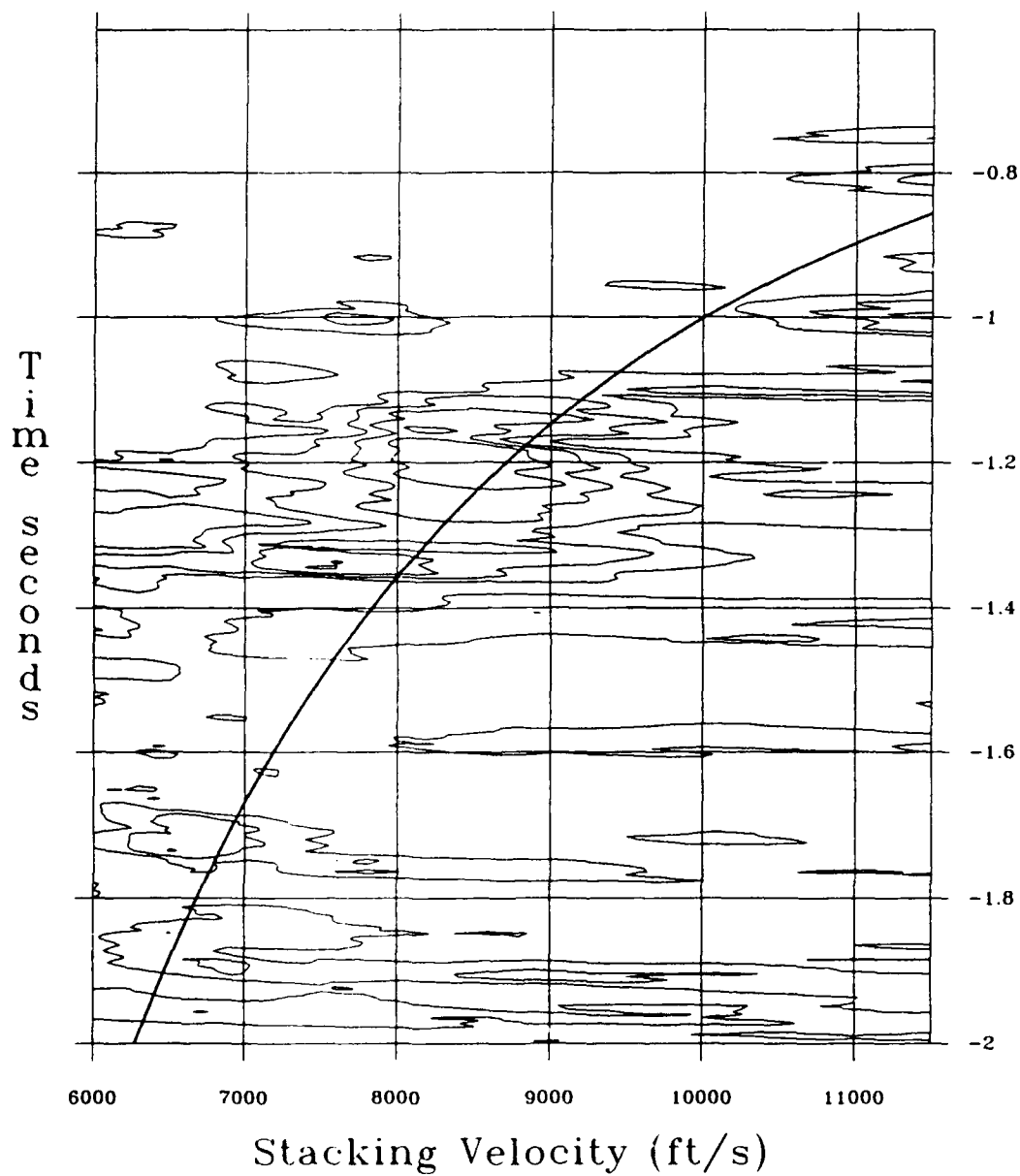
Stacking Velocity Analysis
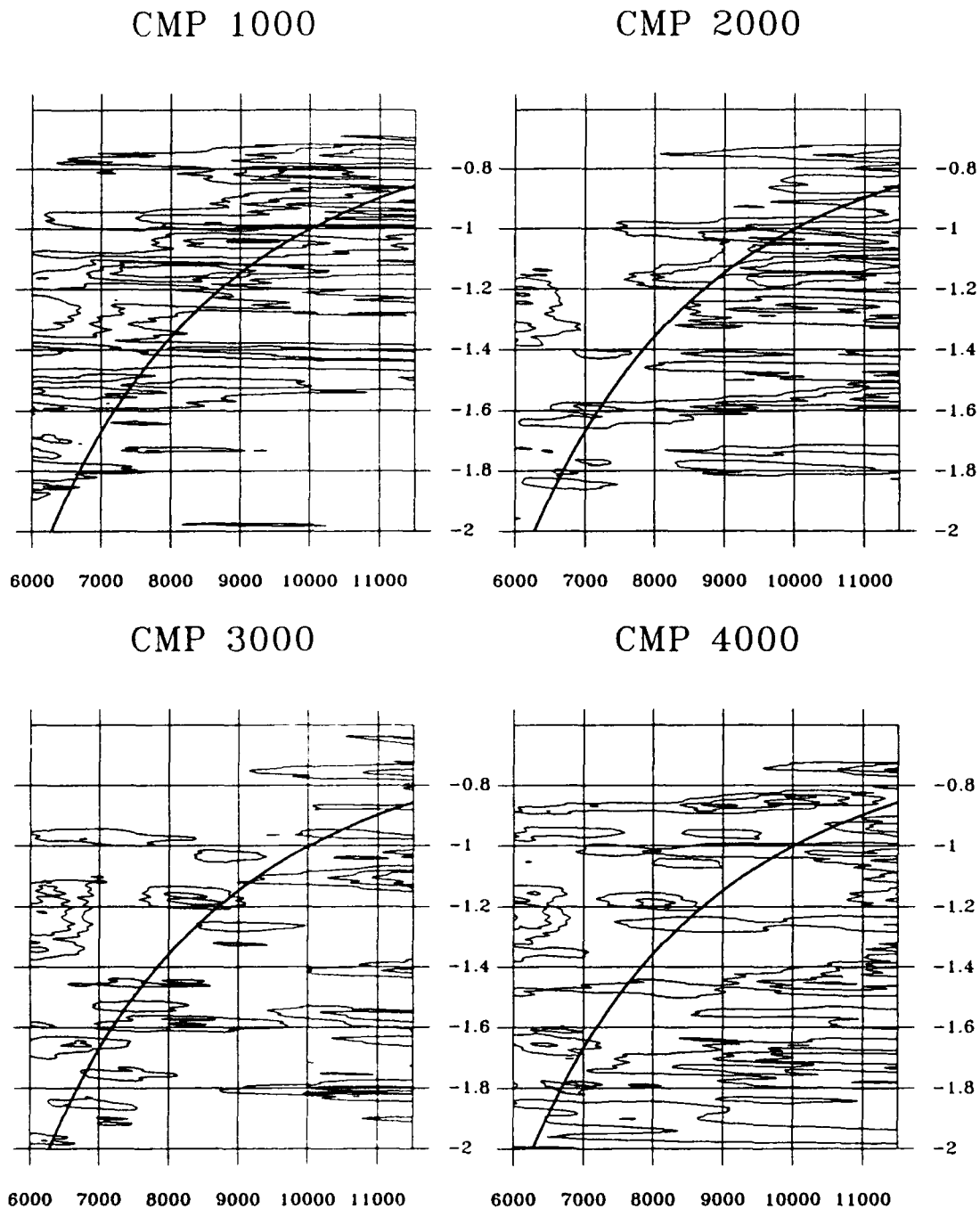

Stacking Velocity (ft/s)

Figure 3.5: Stacking velocity analysis of Figure 3.4. ⁚ PSSP event should be a peak on or near the curved line.

Figure 3.6: Stacking velocity analysis of dip filtered CMP gathers. A PSSP event should be a peak on or near the curved line.
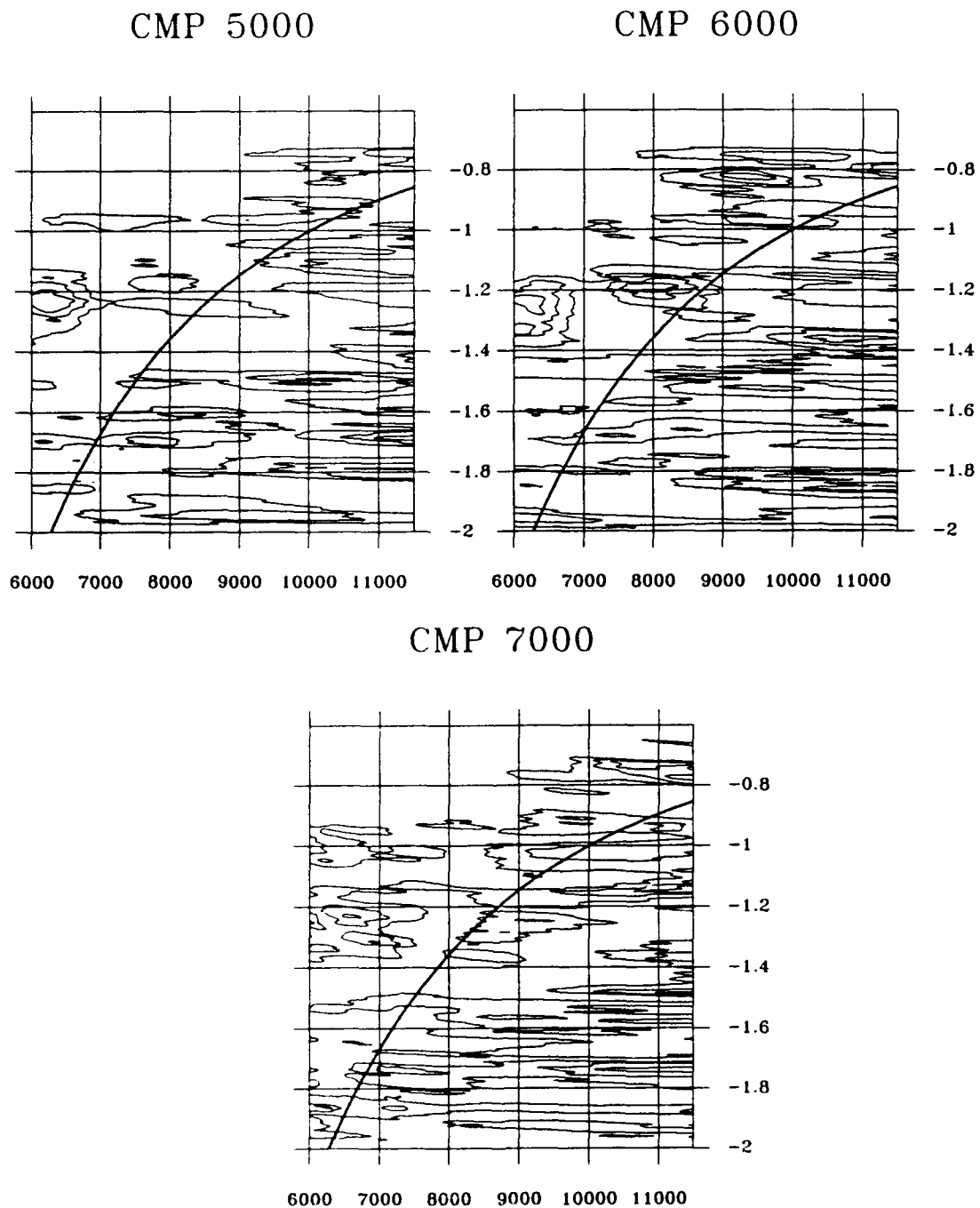
CMP 5000

CMP 6000

CMP 7000

Figure 3.6 (cont.): Stacking velocity analysis of dip filtered CMP gathers. A PSSP event should be a peak on or near the curved line.

Stack After Dip Filter v=8000
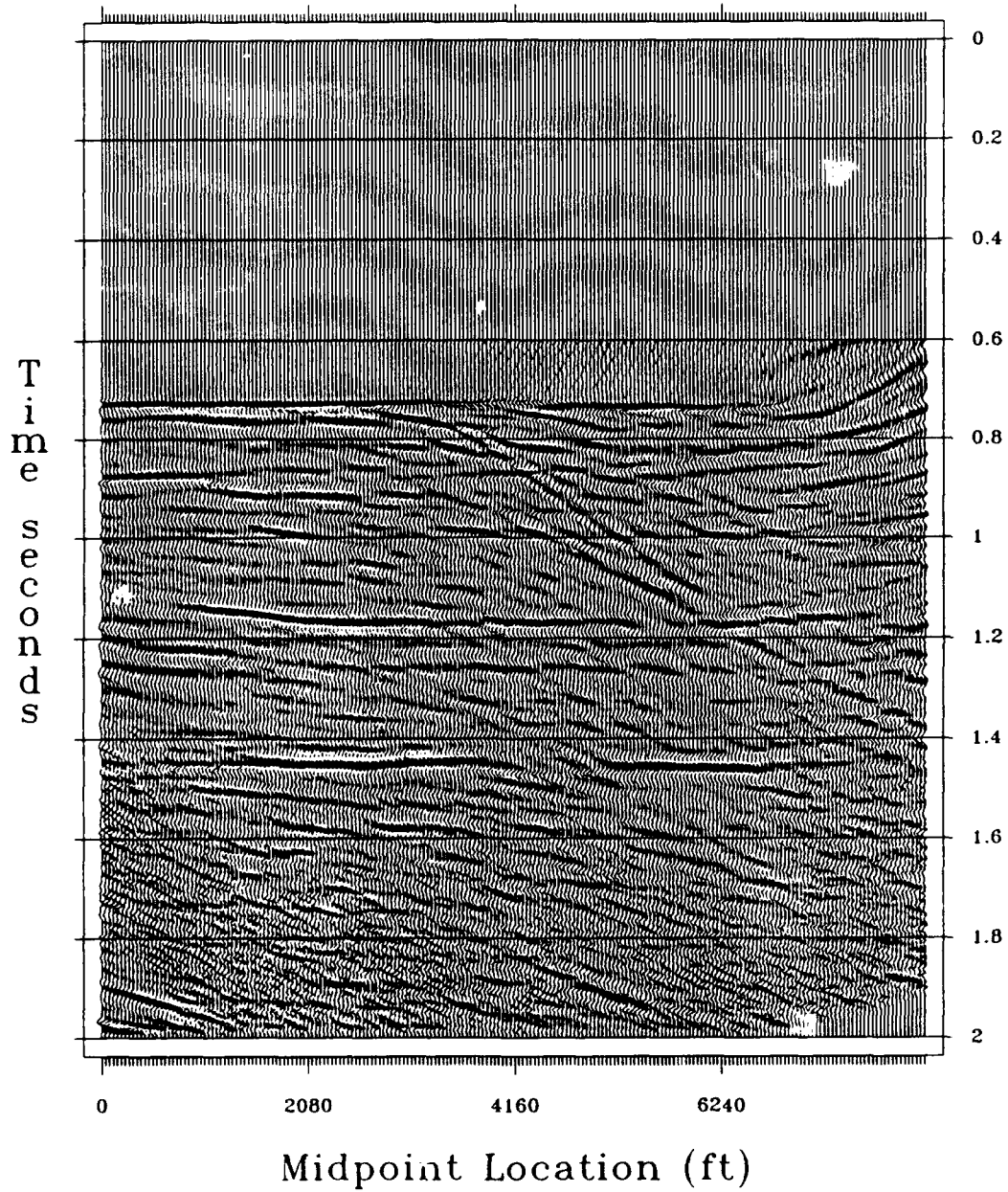
Figure 3.7: Constant velocity stack with $v_s = 8000$ feet/s. AGC has been applied.

P–S Transmission Coefficient
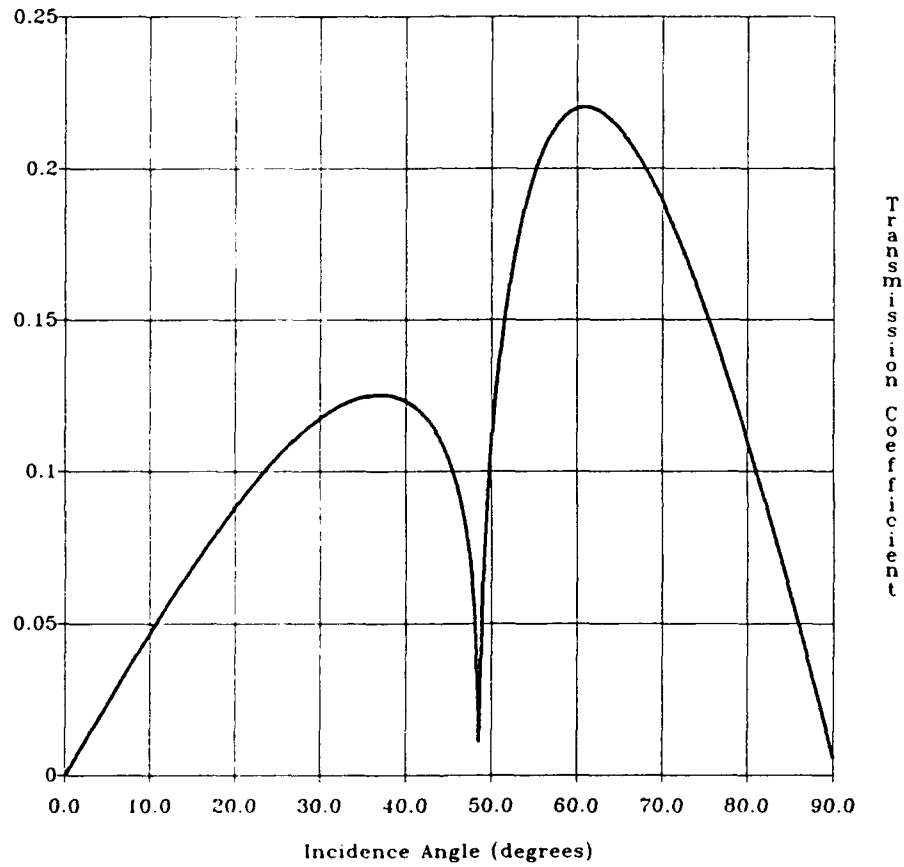
Figure 3.8: P to S transmission coefficient with $c = 11750$ ft/s, $c_1 = 15750$ ft/s, and $b_1 = 0.3c_1$. There is no density contrast. More conversion occurs for incidence angles greater than the critical angle of $48°$.

S–P Transmission Coefficient

Figure 3.9: S to P transmission coefficient with the same parameters as in Figure 3.8. Most conversion occurs for emergence angles greater than the critical angle of 48°.

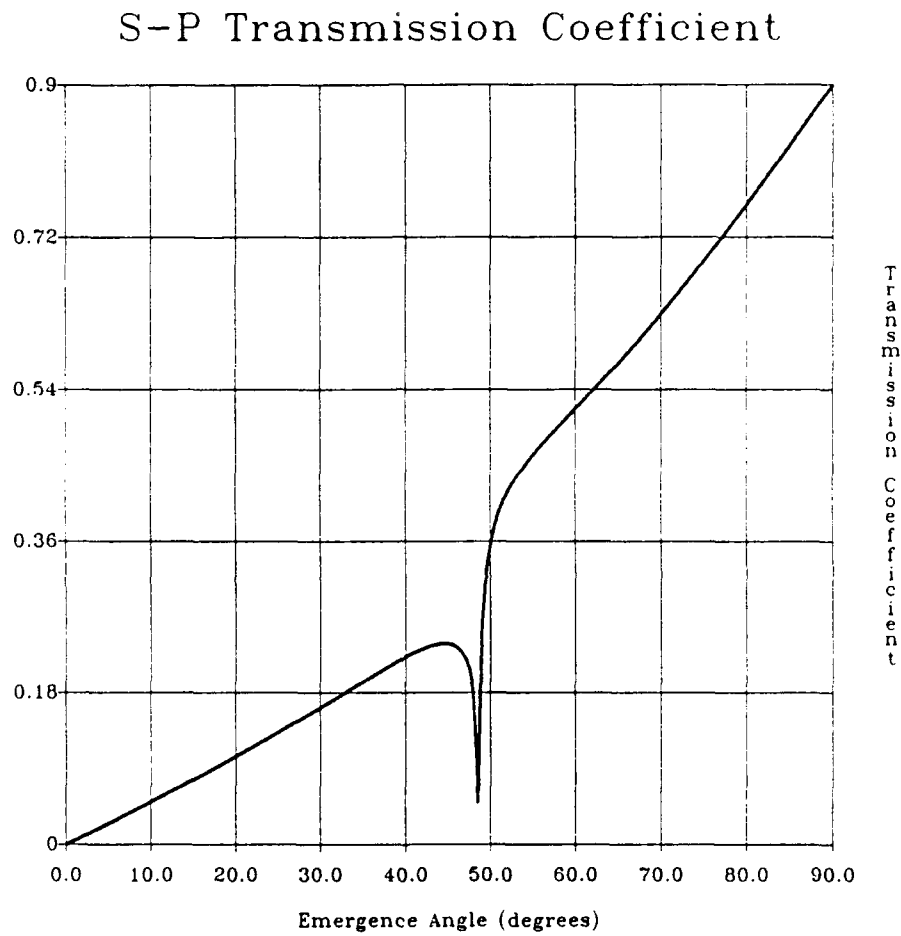# REPORT DOCUMENTATION PAGE

1a. REPORT SECURITY CLASSIFICATION Unclassified		1b. RESTRICTIVE MARKINGS None			
2a. SECURITY CLASSIFICATION AUTHORITY		3. DISTRIBUTION/AVAILABILITY OF REPORT			
2b. DECLASSIFICATION/DOWNGRADING SCHEDULE					
4. PERFORMING ORGANIZATION REPORT NUMBER(S) CWP-083		5. MONITORING ORGANIZATION REPORT NUMBER(S)			
6a. NAME OF PERFORMING ORGANIZATION Center for Wave Phenomena Colorado School of Mines	6b. OFFICE SYMBOL (If applicable)	7a. NAME OF MONITORING ORGANIZATION Mathematical Sciences Division Office of Naval Research			
6c. ADDRESS (City, State, and ZIP Code) Golden, CO 80401		7b. ADDRESS (City, State, and ZIP Code) 800 N. Quincy Street Arlington, VA 22217-5000			
8a. NAME OF FUNDING/SPONSORING ORGANIZATION	8b. OFFICE SYMBOL (If applicable)	9. PROCUREMENT INSTRUMENT IDENTIFICATION NUMBER N00014-88-K-0092			
8c. ADDRESS (City, State, and ZIP Code)		10. SOURCE OF FUNDING NUMBERS			
		PROGRAM ELEMENT NO	PROJECT NO	TASK NO	WORK UNIT ACCESSION NO

11. TITLE (Include Security Classification)

Common Shot, Prestack Inversion and Mode Conversion Analysis of Physical Model Seismic Data

12. PERSONAL AUTHOR(S)
Mark Jeffrey Emanuel

13a. TYPE OF REPORT Technical	13b. TIME COVERED FROM _____ TO _____	14. DATE OF REPORT (Year, Month, Day) August 1989	15. PAGE COUNT 61

16. SUPPLEMENTARY NOTATION

Submitted for publication in Geophysics.

17.	COSATI CODES		18. SUBJECT TERMS (Continue on reverse if necessary and identify by block number)
FIELD	GROUP	SUB-GROUP	

19. ABSTRACT (Continue on reverse if necessary and identify by block number)

See reverse side.

20. DISTRIBUTION/AVAILABILITY OF ABSTRACT ☒ UNCLASSIFIED/UNLIMITED ☐ SAME AS RPT ☐ DTIC USERS	21. ABSTRACT SECURITY CLASSIFICATION	
22a. NAME OF RESPONSIBLE INDIVIDUAL Norman Bleistein	22b. TELEPHONE (Include Area Code) (303) 273-3557	22c. OFFICE SYMBOL

DD FORM 1473, 84 MAR

83 APR edition may be used until exhausted
All other editions are obsolete

☆ U.S. Government Printing Office 1986—607-044

ABSTRACT

Imaging physical model data provides a good test for an inversion algorithm. The physical model data are real wave fields and do not include the simplifications of synthetic data. Also, the parameters of the model are known beforehand so that it is easy to determine how well the inversion works. Here, inversion is a true amplitude Kirchhoff depth migration in the sense that the amplitude of the imaged reflections is proportional to the reflection coefficient. Each shot record in a physical model data set is inverted separately with a common shot, prestack inversion routine with a laterally and depth variable velocity function. Each shot record inversion forms a partial image of the subsurface. The results are then stacked to form a full image of the subsurface. The physical model data set is inverted twice. For the second inversion, the output trace spacing is half the spacing for the first inversion and the output aperture is three times wider than in the first inversion. In both cases, the background velocity field is nearly identical to the actual model. This tests the inversion procedure independent of velocity analysis. Both inversions accurately position reflectors in the model but each performs better on different portions of the data. With a larger inversion output zone, steeper events are imaged better but the increased migration "smile" noise obliterates some deeper events. Both inversions are superior to a migration of the data performed by Marathon Oil Company. Velocities and densities of the model were estimated from the inversion amplitudes. The estimated velocities from the two uppermost reflectors agreed within ten precent of the true velocities but the estimates degraded with the deeper reflectors. The accuracy of the density estimates could not be determined because the true densities were unavailable.

The physical model data are also analyzed for doubly mode-converted reflections. The data are dip filtered to try to separate any mode converted reflections from primary compressional wave reflections. Stacking velocity analysis is used to determine whether the dip-filtered data contain any mode converted reflections. No mode converted energy is evident in the data.